

2

**D-A239 212**



# **RESPONSE OF PROPELLANT COMBUSTION TO UNSTEADY TURBULENT FLOWS**

**Robert A. Beddini  
Ted A. Roberts**

**University of Illinois at  
Urbana-Champaign  
506 S. Wright Street  
Champaign IL 61820**

**June 1991**

**Final Report**

**APPROVED FOR PUBLIC RELEASE; DISTRIBUTION UNLIMITED.**



**PHILLIPS LABORATORY  
Propulsion Directorate  
AIR FORCE SYSTEMS COMMAND  
EDWARDS AIR FORCE BASE CA 93523-5000**

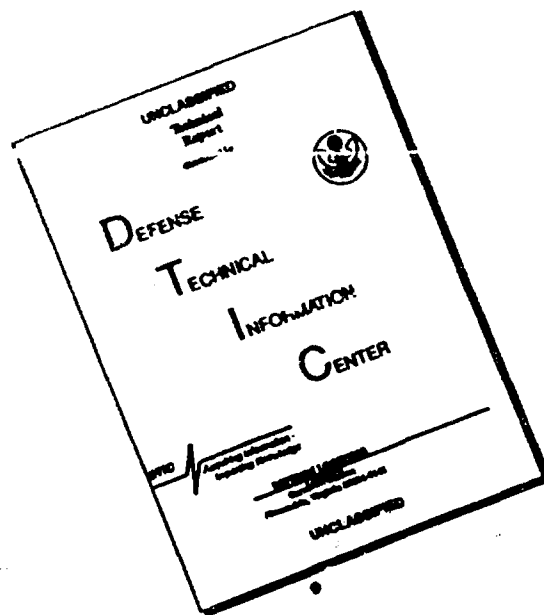
**91-07169**



91

039

# DISCLAIMER NOTICE



THIS DOCUMENT IS BEST  
QUALITY AVAILABLE. THE COPY  
FURNISHED TO DTIC CONTAINED  
A SIGNIFICANT NUMBER OF  
PAGES WHICH DO NOT  
REPRODUCE LEGIBLY.

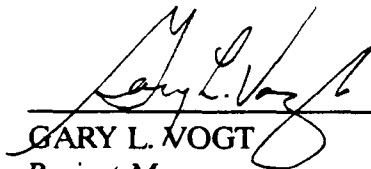
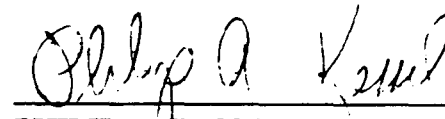
## NOTICE

When U.S. Government drawings, specifications, or other data are used for any purpose other than a definitely related Government procurement operation, the fact that the Government may have formulated, furnished, or in any way supplied the said drawings, specifications, or other data, is not to be regarded by implication or otherwise, or in any way licensing the holder or any other person or corporation, or conveying any rights or permission to manufacture, use or sell any patented invention that may be related thereto.

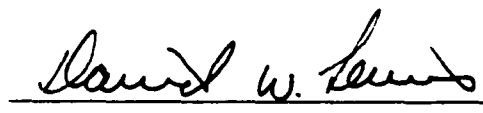

## FOREWORD

This final report was submitted by the University of Illinois at Urbana-Champaign, Champaign IL on completion of contract F04611-86-K-0081 with the OLAC, Phillips Laboratory (AFSC) (formerly Astronautics Laboratory), Edwards AFB CA 93523-5000. OLAC PL Project Manager was Gary L. Vogt.

This report has been reviewed and is approved for release and distribution in accordance with the distribution statement on the cover and on the DD Form 1473.

  
\_\_\_\_\_  
GARY L. VOGT  
Project Manager  
\_\_\_\_\_  
PHILIP A. KESSEL  
Chief, Thermophysics Branch

## FOR THE COMMANDER

  
\_\_\_\_\_  
DAVID W. LEWIS, MAJOR, USAF  
Acting Director  
Fundamental Technologies Division  
\_\_\_\_\_  
RANNEY G. ADAMS  
Public Affairs Director

REPORT DOCUMENTATION PAGE				Form Approved OMB No. 0704-0188	
1a. REPORT SECURITY CLASSIFICATION Unclassified			1b. RESTRICTIVE MARKINGS		
2a. SECURITY CLASSIFICATION AUTHORITY			3. DISTRIBUTION/AVAILABILITY OF REPORT Approved for Public Release: Distribution is Unlimited		
2b. DECLASSIFICATION/DOWNGRADING SCHEDULE					
4. PERFORMING ORGANIZATION REPORT NUMBER(S)  UILUENG 90-053			5. MONITORING ORGANIZATION REPORT NUMBER(S)  AL-TR-90-075		
6a. NAME OF PERFORMING ORGANIZATION University of Illinois at Urbana-Champaign		6b. OFFICE SYMBOL (If applicable)  AAE	7a. NAME OF MONITORING ORGANIZATION Phillips Laboratory Propulsion Directorate		
6c. ADDRESS (City, State, and ZIP Code) 506 S. Wright Street Champaign, IL 61820		7b. ADDRESS (City, State, and ZIP Code) OLAC PL/RFT Edwards AFB CA 93523-5000			
8a. NAME OF FUNDING/SPONSORING ORGANIZATION		8b. OFFICE SYMBOL (If applicable)	9. PROCUREMENT INSTRUMENT IDENTIFICATION NUMBER  F04611-86-K-0081		
8c. ADDRESS (City, State, and ZIP Code)		10. SOURCE OF FUNDING NUMBERS			
		PROGRAM ELEMENT NO. 62302F	PROJECT NO. 5730	TASK NO. OOPP	WORK UNIT ACCESSION NO. 342020
11. TITLE (Include Security Classification) Response to Propellant Combustion to Unsteady Turbulent Flows (U)					
12. PERSONAL AUTHOR(S) Beddini, Robert A. and Roberts, Ted A.					
13a. TYPE OF REPORT FINAL TECHNICAL		13b. TIME COVERED FROM 86-08-01 TO 90-12-31	14. DATE OF REPORT (Year, Month, Day) 9106		15. PAGE COUNT 64
16. SUPPLEMENTARY NOTATION Propulsion Directorate formerly known as the Astronautics Laboratory (AFSC).					
17. COSATI CODES			18. SUBJECT TERMS (Continue on reverse if necessary and identify by block number)		
FIELD	GROUP	SUB-GROUP	COMBUSTION INSTABILITY; SOLID PROPELLANT; TRANSPIRATION, ACOUSTIC BOUNDARY LAYER, TURBULENCE, TRANSITION		
21	08	2			
19. ABSTRACT (Continue on reverse if necessary and identify by block number)					
<p>Turbularization of an acoustic boundary-layer (Stokes layer) on impermeable and permeable surfaces is analytically considered. The theoretical approach utilizes a second-order closure model of turbulence. Both an approximate, closed-form solution and a more comprehensive finite difference solution of the time dependent, parabolic, one-dimensional governing equations are obtained. For simple acoustic boundary-layers on impermeable surfaces, both the approximate solution and the numerical results for the critical acoustic Mach number required for turbulent transition are qualitatively confirmed by experiment. The calculations for acoustic boundary-layers with transpiration (injection) indicate a substantial reduction of the acoustic Mach number required for transition for small values of the normalized injection velocity. The results may provide a mechanism for flow-related combustion instability in practical systems, particularly solid propellant rockets, since turbularization of the near-surface combustion zone could result at relatively low acoustic Mach numbers.</p> <p>(Abstract continued on next page)</p>					
20. DISTRIBUTION/AVAILABILITY OF ABSTRACT <input checked="" type="checkbox"/> UNCLASSIFIED/UNLIMITED <input type="checkbox"/> SAME AS RPT <input type="checkbox"/> DTIC USERS			21. ABSTRACT SECURITY CLASSIFICATION UNCLASSIFIED		
22a. NAME OF RESPONSIBLE INDIVIDUAL Gary Vogt			22b. TELEPHONE (Include Area Code) 805-275-5258		22c. OFFICE SYMBOL RFT

## 19. ABSTRACT- continuation

An analysis of the transitional and turbulent reactive acoustic boundary layer on a homogeneous solid-propellant surface is conducted to investigate potential mechanisms of combustion instability. A new technique is developed for the condensed-phase thermal layer, in which the propellant space is mapped onto the gas space and efficiently solved using the same adaptive numerical grid. Results are obtained at an acoustic pressure node in the absence of a mean axial flow. The results indicate that acoustically induced transition can occur at relatively low acoustic pressure amplitudes, propellant response to harmonic axial velocity fluctuations is rectified and results in a mean augmentation ("D-C shift"), and that nominal propellant combustion parameters lead to increasing susceptibility to acoustic transition at elevated mean pressures.

Further analysis of the the turbulent reactive acoustic boundary layer on a homogeneous solid propellant surface is conducted to investigate the variation of acoustic erosion (the time - mean augmentation of propellant burning rate due to the acoustic motion) along the length of the chamber of a solid rocket motor or center - vented T-burner. An order - of - magnitude analysis indicates that the enthalpy and species equations remain similar in the presence of acoustic pressure oscillations. Results are obtained throughout the length of the chamber in the absence of a mean axial flow. The results indicate that the increase in mean burn rate (DC-shift) observed in many T-burner experiments may be due to turbularization of the acoustic boundary-layer above the burning propellant. A comparison is made between predicted and experimental response functions for acoustic and steady-state erosive burning. The threshold axial velocity for acoustic erosion is found to be significantly lower than that of steady-state erosion, and the amplitude and harmonic content of the propellant response varies considerably throughout the chamber.

## TABLE OF CONTENTS

	page
LIST OF FIGURES	iv
NOMENCLATURE	vi
INTRODUCTION	1
OVERVIEW - ACOUSTIC INSTABILITY	1
OVERVIEW - ACOUSTIC EROSION	3
RESEARCH OBJECTIVES	3
ANALYSIS	5
DECOMPOSITION OF DEPENDENT VARIABLES	5
ORDER-OF-MAGNITUDE ANALYSIS	5
COMPUTATIONAL ANALYSIS	10
RESULTS AND DISCUSSION	17
STABILITY OF ISOTHERMAL ACOUSTIC BOUNDARY LAYERS	17
REACTIVE ACOUSTIC BOUNDARY LAYER - PRESSURE NODE	25
COMBINED RESPONSE AT VARIOUS AXIAL LOCATIONS	34
COMPARISON OF ACOUSTIC AND STEADY-STATE EROSIVE BURNING	42
CONCLUSIONS	47
REFERENCES	51
APPENDIX A: TABLE OF ASSUMPTIONS	54
APPENDIX B: TABLE OF PROPELLANT PARAMETERS	55
APPENDIX C: PUBLICATIONS	56

## LIST OF FIGURES

	page
Figure 1. Mean flow and acoustic profiles at a pressure node.	4
Figure 2. Transition to turbulence for simple acoustic motion.	9
Figure 3. Laminar velocity profiles in the acoustic boundary layer without injection.	18
Figure 4. Turbulent velocity profiles in the acoustic boundary layer without injection.	19
Figure 5. Turbulence intensity profiles in the acoustic boundary layer without injection.	19
Figure 6. Turbulent velocity profiles in the acoustic boundary layer with injection.	20
Figure 7. Turbulence intensity profiles in the acoustic boundary layer with injection.	20
Figure 8. Effect of injection on the stability of the acoustic boundary layer.	22
Figure 9. Effects of injection and injection disturbance level on the stability of the acoustic boundary layer.	23
Figure 10 (a-c). Time variation of turbulence development for the injected acoustic boundary layer ( $\sigma_v = 0$ , $y = \delta_a$ ).	24
Figure 11 (a-c). Time variation of turbulence development for the injected acoustic boundary layer ( $\sigma_v = 0.035$ , $y = \delta_a$ ).	25
Figure 12. Steady state temperature profiles.	26
Figure 13. Comparison of temperature and turbulent velocity profiles at various times within a cycle.	28
Figure 14. Comparison of corresponding temperature and turbulence intensity profiles at various times within a cycle.	28
Figure 15. Critical acoustic Reynolds number required for transition.	29
Figure 16. Variation of critical pressure ratio required for transition as a function of mean chamber pressure.	30

Figure 17.	Variation of propellant response as a function of time for various surface roughness heights.	32
Figure 18.	Variation of propellant response as a function of time for endo- and exothermic surface decomposition energies.	32
Figure 19.	Harmonic content of the propellant responses shown in Figure 16 for a smooth and rough wall ( $k_s = 0$ and $k_s = 150$ mm, respectively)	33
Figure 20.	Relative phase angle of the responses shown in Figure 16.	33
Figure 21.	Normalized steady-state temperature profiles.	35
Figure 22.	Comparison of normalized temperature perturbations with and without the similarity assumption.	36
Figure 23.	Normalized laminar and turbulent gas-phase temperature perturbations.	37
Figure 24.	Normalized laminar and turbulent gas-phase normal velocity perturbations.	38
Figure 25.	Normalized laminar and turbulent condensed-phase temperature perturbations.	39
Figure 26.	Combined response of the condensed-phase regression rate as a function of axial location.	40
Figure 27.	Harmonic content of the combined response versus axial location for $\Pi_{ma} = 0.05$ , $f = 1000$ Hz, and $k_s = 150$ mm).	41
Figure 28.	Acoustic erosion vs axial location within the chamber for various equivalent sand roughness heights.	44
Figure 29.	Experimental comparison of acoustic and steady-state erosion (after Ref. 14.)	44
Figure 30.	Comparison of calculated acoustic and steady-state erosion.	45
Figure 31.	Comparison of calculated acoustic erosion at acoustic oscillations of 1000 Hz and 2000 Hz.	46



## NOMENCLATURE

$a_0$	unperturbed sonic speed
$A_s$	pre-exponential constant in surface reaction
$B_g$	pre-exponential constant in gas phase reaction
$c_p$	specific heat at constant pressure
$c_\pi$	specific heat of condensed phase
$f$	frequency, Hz
$h$	specific sensible enthalpy
$h_\alpha^0$	heat of formation of species $\alpha$
$H$	total enthalpy, $h + u^i u_i / 2$
$k$	thermal conductivity
$k_s$	equivalent sand roughness height
$L_s^0$	heat of (dissociative) evaporation or sublimation
$M$	Mach number defined using $a_0$
$n$	normal burning rate pressure exponent
$p$	static pressure
$q$	turbulence intensity, $(\overline{u^i u_i})^{1/2}$
$r$	radial distance from centerline
$\dot{r}$	condensed phase surface regression rate
$R$	inner radius of a cylindrical duct
$Re_{ac}$	axial acoustic Reynolds Number, $\overline{u}_c / (f / \overline{v}_c)^{1/2}$
$Re_s$	injection Reynolds number, $\overline{\rho}_s \overline{v}_s \delta / \overline{\mu}_s$
$Re_t$	turbulence Reynolds number, $\overline{\rho} q \Lambda / \mu$
$R_u$	universal gas constant
$t$	time
$T$	static temperature
$T_A$	activation temperature
$u_j$	velocity vector ( $u, v, w$ )
$W_{av}$	average molecular weight
$x_j$	coordinate vector
$y$	distance from surface, $\delta - r$ , (planar flow); or $R - r$ , axisymmetric flow
$Y_\alpha$	species mass fraction
$\alpha$	index for chemical species
$\alpha_\pi$	thermal diffusivity of the condensed phase, $k_\pi / (\rho_\pi c_\pi)$

$\beta_g$	temperature exponent of gas phase reaction pre-exponential coefficient
$\delta_a$	non-injected, laminar acoustic boundary-layer thickness, $(\nu/f)^{1/2}$
$\delta_{aa}$	actual injected acoustic boundary-layer thickness
$\delta_f$	normalized flame height, $k_s/\dot{m} c_p$
$\Delta h_g$	heat of reaction per unit mass
$\eta$	condensed phase coordinate
$\phi$	characteristic length scale
$\Phi$	concentration (pressure) exponent in reaction rate
$\Lambda$	turbulence macro-length scale
$\Pi$	relative static pressure amplitude $ p'' /\bar{p}$
$\mu$	viscosity
$\nu$	kinematic viscosity
$\rho$	density
$\sigma$	$= k/c_p$
$\sigma_v$	$= [\overline{v'_s v'_s} / \bar{v}_s^2]^{1/2}$
$\tau$	normalized time, $f t$ , cycles
$\upsilon$	index for planar or axisymmetric geometry
$\omega$	specific reaction source term
$\zeta_\pi$	linear stretching factor used in condensed phase mapping

### Superscripts and Operators

$\overline{\phantom{x}}$	average of variable over turbulent fluctuations
$\langle \phantom{x} \rangle$	time mean of variable
$'$	turbulent fluctuation value of variable
$''$	acoustic fluctuation value of variable
$*$	reference condition

### Subscripts

a	acoustic
c	duct centerline
e	value at edge of boundary layer
f	value at edge of flame zone
g	gas phase
h	condition at port head end
l	value of variable at local axial position
m	maximum absolute value

$s$	condition at surface
ss	steady-state value of variable
$\pi$	condensed phase, propellant

## INTRODUCTION

### OVERVIEW - ACOUSTIC INSTABILITY

Oscillatory flows in ducts can be sustained by a variety of interactions. These range from purely fluid-dynamically induced motions (e.g., large scale vortex shedding or shockwave instability), to the more energetic motions possible with diabatic flows. Particularly severe oscillations can occur in solid propellant rocket chambers, for example, wherein the oscillatory motion can be driven by interactions with the substantial energy release inherent in near-surface combustion processes.

Prior analytical work in combustion instability in solid rockets has identified some of the mechanisms which can produce acoustic velocity coupling to the overall instability process (see, for example, Culick<sup>1,2</sup>). These studies have shown that for a simple longitudinal standing acoustic wave in a duct, a Rayleigh diabatic instability criterion can result which is dependent upon the oscillatory motion of the gas column. Since the energy release occurs in the near surface region, analytical work has addressed acoustic boundary-layer effects on propellant combustion response (see, for example, Lengele<sup>3</sup>). Implicit in several response function analyses is the assumption that the acoustic boundary-layers behave quasi-steadily and in phase with the longitudinal acoustic velocity outside the boundary layer.

Recent work on combustion-flowfield interactions in solid rocket chambers has analytically and experimentally examined fundamental fluid-dynamic aspects of mean flow, acoustic wave and turbulence behavior. Hydrodynamically modeling the flow with a semi-enclosed, porous-walled duct (with large injection through the wall), Brown et al<sup>4</sup> experimentally confirmed the transitional behavior of the mean flow predicted by Beddini<sup>5</sup>. The major emphasis of this non-reactive flow experiment was to investigate the effect of low and moderate amplitude forced acoustic oscillations on the flow, using both hot-wire anemometry and surface-mounted hot-film sensors.

Basing their conclusions on the surface sensor measurements, Brown, et al<sup>4</sup> suggested that near surface turbulence produced by the mean-flow transition process appeared to "destroy" the coherent response of the sensors downstream of

nsition. Consequently, for low acoustic amplitudes, a surface response capable of inducing instability would most probably originate in the head end (pre-transition) of a rocket chamber. However, it is noted that for large axial distances, low amplitude acoustic signals appear to be resurrected in the post transition region. Lower amplitude harmonics of the driving frequency were observed by Brown in both the surface and hot wire measurements. Their existence is consistent with the nonlinear behavior of a (potentially thick) acoustic boundary layer (Stokes layer).

Analyses of laminar acoustic boundary-layer phenomena involved in propellant response have been offered by Flandro<sup>6</sup>; Glick and Renie<sup>7</sup>; Ben Reuven<sup>8</sup> and Hedge, et al.<sup>9</sup>. Zinn and colleagues<sup>10</sup> have obtained Schlieren and radiation measurements for a premixed reactive Stokes Layer on a porous plate. Baum and Irvine<sup>11</sup> utilized a full unsteady Navier-Stokes solution method; their results showed a Stokes layer persisting even in the presence of strong injection velocities. The thickness of the Stokes layer was of the same order as the Stokes layer for noninjected flow. The presence of vortices above the acoustic boundary layer were also indicated in the results. Although several aspects of these analyses are interesting, the following important point is noted. Simple scaling estimates of the laminar acoustic boundary layer height (the Stokesian thickness)  $\delta_a = \sqrt{\nu/f}$  indicate that  $\delta_a$  is well above the gas-phase flame height except for very high frequencies ( $f \geq 10^4$  Hz). Consequently, minimal acoustic velocity interaction with combustion would be expected at low to intermediate frequencies, as indicated, for example, by the more detailed analysis of Flandro<sup>6</sup>. Although this does not preclude locally-coupled instability resulting from laminar interactions (whether linear or nonlinear), it does suggest that other mechanisms of interaction should be explored.

It is well established that for piston driven closed duct flows (viz., in which there is negligible mean axial flow), longitudinal acoustic waves of a few percent relative pressure amplitude can induce turbulence within the Stokes layer. The literature review and independent data of Merkli and Thomann<sup>12</sup>, for example, confirm a critical amplitude which varies as  $\sqrt{f}$  for this type of simple acoustic excitation. Thus, for fixed amplitude, lower frequency disturbances are more likely to induce turbulence.

It is known from studies of quasi-steady solid propellant/flowfield interactions that even small levels of turbulence within the combustion zone can

appreciably enhance propellant combustion rates, predominantly by increasing heat transfer from the flame zone back to the propellant surface. Whether acoustically induced turbularization can occur in actual rocket chambers depends upon several complex effects including the presence of large injection rates, surface roughness, and of course, the specific type of combustion process. In one experiment<sup>13</sup>, values of the threshold velocity for propellant response (acoustic erosivity) were lowered by a factor of two relative to steady state conditions. Acoustic turbularization of the propellant combustion zone was also suspected by Medvedev and Revyagin<sup>14</sup>, based on their T-burner data and the data of Price<sup>15</sup>.

## OVERVIEW - ACOUSTIC EROSION

Solid rocket motors are susceptible to several types of flowfield related combustion anomalies. Steady-state erosion and acoustic coupling are examples of combustion enhancements which can lead to anomalous burning or, in some instances, catastrophic failure of the motor due to increased chamber pressures. The steady-state erosive burning problem (also referred to herein as erosive combustion or steady-state erosion) has been addressed in past studies and is generally believed to be a consequence of the *turbulent mean flowfield enhancing the combustion and heat transfer processes by increasing the effective thermal diffusivity*<sup>16</sup>. Steady-state erosive burning is therefore most likely to occur in rocket motors having large length to diameter ratios in which the flowfields attain large velocities. It has also been known for some time that erosive combustion can occur without the presence of an appreciable mean flowfield, specifically, in acoustic environments found in the center-vented T-burner experiments of Medvedev and Revyagin<sup>14</sup> and Crump and Price<sup>15,17</sup>.

## RESEARCH OBJECTIVES

The objective of the present analysis is to consider, under several simplifying assumptions, the general trends of acoustic boundary-layer turbularization on a permeable surface in the presence of large injection rates. The fundamental nonreactive problem is considered first. The analysis is then extended to include the unsteady heat conduction and combustion of the condensed phase. The phenomena of interest are schematically depicted in Figure 1. General trends of

reactive acoustic boundary-layer turbularization on a propellant surface under nominal homogenous propellant conditions are investigated together with the resulting response.

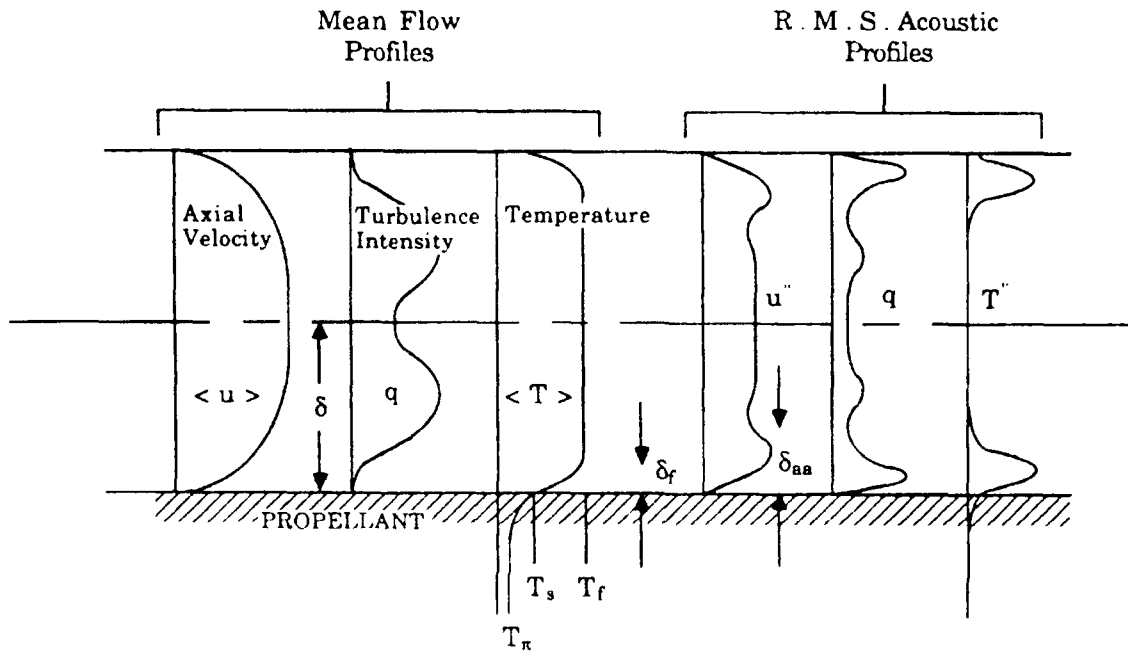


**Figure 1. Mean flow and acoustic profiles at a pressure node.**

The combined response of solid propellant combustion, due to both acoustic pressure oscillations and the accompanying turbulent flow, is also investigated. Under several simplifying assumptions, the general trends of the combined response of the solid propellant at various positions within a center vented T-burner, or low Mach number region of a solid rocket, are determined. A comparison of acoustic and steady-state erosive combustion response is also performed, since a close relation between these phenomena has been assumed in prior studies<sup>2</sup>.

## ANALYSIS

### DECOMPOSITION OF DEPENDENT VARIABLES

The motion of a perfect gas described by the Navier-Stokes equations is considered. An arbitrary dependent variable,  $g(x_i, t)$ , is decomposed according to the notation

$$g(x_i, t) = \bar{g}(x_i, t) + g'(x_i, t)$$

with

$$\bar{g} = \langle g(x_i, t) \rangle + g''(x_i, t).$$

In these equations,  $g'$  is the turbulent fluctuation,  $\bar{g}$  is the ensemble average,  $g''$  is the acoustic (deterministic) component and  $\langle g \rangle$  is the long-time mean. The remainder of this section is divided into two parts, the first considering order-of-magnitude analysis of the problem and derivation of an approximate relation for critical amplitude of transition from the turbulence model equations. The second part discusses the equations and method used for a more comprehensive numerical solution of the acoustic boundary-layer in the presence of transpiration.

### ORDER-OF-MAGNITUDE ANALYSIS <sup>18</sup>

Neglecting third order correlations and the axial derivatives of molecular and turbulent stresses, the  $\langle \rangle$  average of the axial momentum equation is

$$\frac{\partial}{\partial x} (\langle \rho \rangle \langle u \rangle \langle u \rangle + \langle \rho \rangle \langle u'' u'' \rangle + \langle u \rangle \langle \rho'' u'' \rangle + \langle u \rangle \langle \rho'' u'' \rangle)$$

$$+ \frac{\partial}{\partial y} (\langle \rho \rangle \langle u \rangle \langle v \rangle + \langle \rho \rangle \langle u'' v'' \rangle + \langle u \rangle \langle \rho'' v'' \rangle + \langle v \rangle \langle \rho'' u'' \rangle)$$

$$= \frac{\partial \langle \rho \rangle}{\partial x} + \frac{\partial (\langle \mu \rangle \frac{\partial \langle u \rangle}{\partial y})}{\partial y} + \frac{\partial \langle \tau \rangle}{\partial y} \quad (1)$$



where the mean turbulent shear stress is  $\langle \tau \rangle = -\langle \rho \rangle \langle u'v' \rangle$  (neglecting turbulent density correlations). The equation for the acoustic component ( $u''$ ) is, to first order:

$$\begin{aligned} & \langle \rho \rangle \frac{\partial u''}{\partial t} + (\langle \rho \rangle u'' + \langle u \rangle \rho'') + u'' \frac{\partial}{\partial x} (\langle \rho \rangle \langle u \rangle) \\ & + \langle \rho \rangle \langle u \rangle \frac{\partial u''}{\partial x} + (\langle \rho \rangle v'' + \langle v \rangle \rho'') \frac{\partial \langle u \rangle}{\partial y} \\ & + u'' \frac{\partial}{\partial y} (\langle \rho \rangle \langle v \rangle) + \langle \rho \rangle \langle v \rangle \frac{\partial u''}{\partial y} = - \frac{\partial p''}{\partial x} + \frac{\partial}{\partial y} (\langle \mu \rangle \frac{\partial u''}{\partial y}) + \frac{\partial \tau''}{\partial y} \end{aligned} \quad (2)$$

where  $\tau'' \equiv -\langle \rho \rangle \overline{u'v'}$ .

In equation (1), the second-order correlations arising from the unsteady motion can produce virtual stresses and convective fluxes analogous to those produced by the turbulent motion alone. These correlations induce the classical phenomenon of "acoustic streaming",<sup>19,20</sup> wherein a component of the mean flow is driven by acoustic motion. Of potentially more importance to propellant combustion are the analogous second-order terms which appear in the equation for the transport of thermal energy in the propellant flame zone. While these thermal transport effects will not be analyzed in this study, examples of their importance to effective steady-state heat transfer may be found in the literature (see, for example, Ref. 21). The effects of steady-state enhancements to heat transfer from acoustic streaming effects have not been considered with respect to the reactive environment in rocket engines, although it is possible that these effects could also produce a coupling mechanism for instability.

The remainder of this analysis will be concerned with equation (2) and the relative importance of various terms within the acoustic boundary layer. To further simplify this equation, it will be assumed that the density in the region of interest is approximately constant and that the transverse velocity,  $v''$ , produced by propellant

response is negligible. These assumptions would necessarily be removed in considering a more comprehensive propellant velocity response analysis.

The magnitudes of the terms in Equation (2) are estimated by normalizing the velocities with  $a_0$ , the chamber length with  $L$ , the chamber radius with  $\delta$  and utilizing the continuity equation and the assumption of a standing first longitudinal acoustic mode. It is also assumed that the turbulence shear stress may be scaled by  $\tau'' = c_\tau \langle \rho \rangle u''^2$ , where  $|c_\tau| \ll 1$ . The respective orders of the terms in Equation (2) are then

$$\{1, \langle M \rangle, \langle M \rangle, \langle M \rangle, (\delta_a/\delta) \langle M \rangle, \langle M \rangle, (a_0/f\delta_a) \langle M_s \rangle, 1, v/f\delta_a^2, c_\tau a_0/(f\delta_{a,turb}) M'' \}.$$

The order unity terms (1) and (8) recover the inviscid acoustic mode solution in the central region of the duct. A considerable simplification results if  $\langle M \rangle$  is small, since terms (2) - (6) may be dropped without fundamentally altering boundary layer characteristics retained in terms (7), (9) and (10). (It is important to note that the maximum response to the surface sensors in the experiments of Brown, et al.<sup>4</sup> occurs in the head end region, where  $\langle M \rangle$  is  $\leq 0.1$ .) Neglecting for the moment the transverse convection and turbulence terms, it is seen that for the viscous term to be of order unity implies the Stokes estimate,

$$\delta_a \approx \sqrt{\frac{v}{f}} \quad (3)$$

and is the smallest possible laminar boundary-layer height of the problem. The effects of injection on the acoustic boundary layer [provided largely by term (7)] can be substantial and even dominate. The ratio between the convection and viscous terms in Equation (2) is of the order 10 under conditions of interest.

The additional shear stress provided by term (10) in Equation (2), as well as the analogous additional heat flux appearing in the energy equation, result from possible turbulent motions. Further, it is noted that term (10) is the only retained term which depends on the amplitude of the acoustic motion. (The acoustic amplitude,  $M''$ , is a linear scaling parameter of all other terms but occurs quadratically in the turbulent shear term), thus posing the question of a possible relation to nonlinear stability phenomena.

As noted by Merkli and Thomann<sup>12</sup>, various approaches have been employed to obtain a stability or transition criterion for the acoustic boundary layer. In the approach adopted here, the second-order modeling equations employed in Ref. 5 are considered. Preliminary operations and assumptions are summarized as follows. Equations for the velocity correlations  $\overline{u'_i u'_j}$  are contracted to obtain an equation for the turbulence intensity  $q^2 = \overline{u'_i u'_i}$ . Fluid material properties are assumed constant, and the turbulence (or preturbulent disturbance level) is assumed small so that third and higher order velocity correlations may be neglected. It is also assumed as an approximation that  $\overline{u' u'} = a_{uu} q^2$ ,  $\overline{v' v'} = a_{vv} q^2$ , and  $\overline{u' v'} = a_{uv} q^2$ , where  $a_{uu}$ ,  $a_{vv}$  and  $a_{uv}$  are constants. Substituting these relations into the  $q^2$  equation, taking the mean flow to be negligible, and applying boundary layer assumptions for a quasi-planar condition yields:

$$\begin{aligned} \rho \left( \frac{\partial q^2}{\partial t} + u'' \frac{\partial q^2}{\partial x} + v'' \frac{\partial q^2}{\partial y} \right) + 2\rho q^2 \left( a_{uu} \frac{\partial u''}{\partial y} + a_{uv} \frac{\partial u''}{\partial y} \right) \\ = -2A \mu \frac{q^2}{\Lambda^2} + \mu \frac{\partial^2 q^2}{\partial y^2} \end{aligned} \quad (4)$$

where  $\Lambda$  is the disturbance macrolength - scale and  $A$  is a constant used in modeling low turbulent Reynolds number dissipation. The approximation  $\Lambda = C_\Lambda \delta_a$  (where  $\delta_a$  is specified by Equation (3)), is also employed to evaluate the maximal effective length scale appropriate for the acoustic boundary layer.

Equation (4), which is linear in  $q^2$ , may be order-of-magnitude scaled in the same manner as Equation (2). The requirement that  $\rho(Dq^2/Dt) = 0$  (for neutral stability) may be imposed if the Reynolds number  $u'' \delta_a / \nu \leq 0(1)$ . The order of magnitude analysis indicates that the fifth (production) term on the left hand side and the first (dissipation) term on the right hand side of Equation (4) are dominant, resulting in the stability criterion

$$M_{cr}'' = \frac{A}{(-a_{uv}) C_\Lambda^2} \frac{\sqrt{f} \sqrt{y}}{a_o} = K \frac{\sqrt{f} \sqrt{y}}{a_o} \quad (5)$$

Utilizing the turbulence modeling constants specified in the Appendix of Ref. 5 (i.e.,  $A = 3.25$ ,  $C_A = .17$ ), and estimating  $a_{uv} = -.15$  from fully developed flat-plate turbulent boundary layer flows, yields an estimate of  $K = 750$ . Merkli and Thomann<sup>11</sup> cite prior experimental values of  $K$  ranging from 188 to 915, and obtained the value  $K = 501$  in their own experiments. The constant  $K$  in Equation (5) is related to the Merkli and Thomann constant  $A_c$  by  $K = A_c \sqrt{(2\pi)/2}$ . They speculated that the variation in  $K$  observed in prior studies could be caused by variations in the roughness of the duct surface, and demonstrated that disturbances caused by the anemometer probe can also appreciably affect  $K$ .

The critical Mach number given by Equation (5) is shown in Figure 2 together with the data of Merkli and Thomann. The functional dependence is correct, and even the very approximate estimates of physical constants and empirical parameters yield quantitative agreement to within several percent of the data. To the authors' knowledge, the derivation of an approximate transition relation from linearizing this type of complex turbulence model is novel.

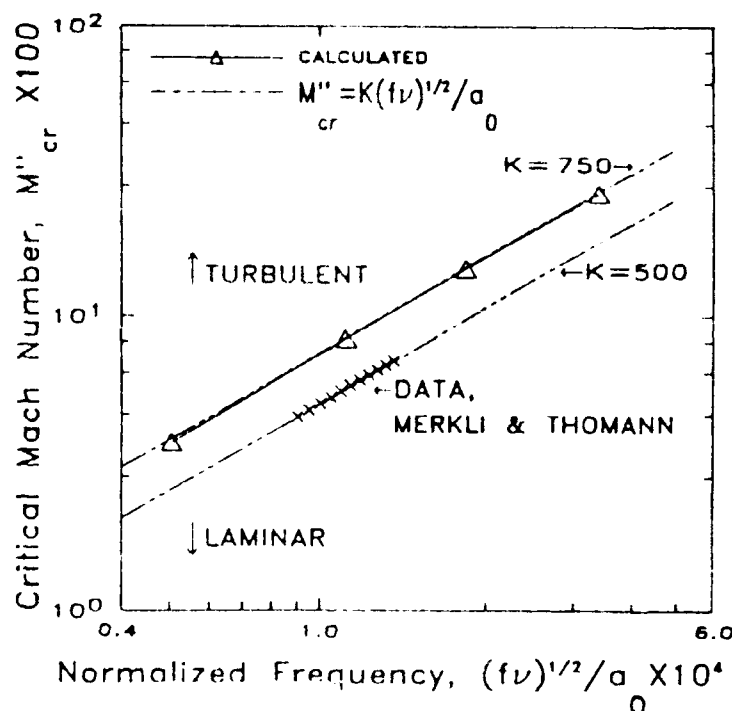


Figure 2. Transition to turbulence for simple acoustic motion.

## COMPUTATIONAL ANALYSIS

The second-order turbulence closure approach developed by Donaldson et al.<sup>22</sup> and Varma et al.<sup>23</sup> was implemented in Ref. 5 as a parabolized model for calculating statistically stationary, compressible transitional flows in porous walled ducts with large injection rates. The assumptions concerning the gas phase are summarized in Appendix A. The assumptions and order-of-magnitude analysis of the previous section again yield a parabolic equation system for the present acoustic boundary-layer problem. Computationally, the axial convection terms  $\overline{\rho u} \partial g / \partial x$  (where  $g$  is an arbitrary dependent variable) are replaced by  $\overline{\rho} \partial g / \partial t$  for the present case. With the exception of  $\partial \overline{\rho} / \partial x$  in the momentum equation, all other axial derivatives are taken to be null. The continuity equation,

$$\frac{\partial \overline{\rho}}{\partial t} + \frac{1}{r^v} \frac{\partial}{\partial r} [r^v \overline{\rho v} + \overline{\rho' v'}] = 0$$

and the  $\partial \overline{\rho} / \partial t$  term on the right hand side of the energy equation are retained, however, for subsequent reactive flow investigations.

The parabolic differential equation system may be considered in the functional form

$$\overline{\rho} \frac{\partial g}{\partial t} + \overline{\rho v} \frac{\partial g}{\partial r} = \frac{1}{r^v} \frac{\partial}{\partial r} (r^v \overline{\mu_g} \frac{\partial g}{\partial r}) + G_g(f) \quad (6)$$

where  $g = \{ \overline{u}, \overline{h}, \overline{u'u'}, \overline{v'v'}, \overline{w'w'}, \overline{u'v'}, \overline{h'u'}, \overline{h'v'}, \overline{h'h'} \}^T$ ,  $u$ ,  $v$  and  $w$  are the axial, radial and circumferential velocity components,  $v$  is the index for planar or axisymmetric geometry,  $\rho$  the density and  $h = c_p T$  is the specific static enthalpy. The molecular transport coefficient  $\mu$  represents the dynamic viscosity ( $\mu$ ) or the thermal conductivity parameter,  $\sigma = k/c_p$ , as appropriate for each equation. However, not all of the molecular diffusion terms for each equation in the system may be cast in the form shown in Equation (2). Those that do not conform are implicitly contained within the complex functions  $G_g$ , which also represent the sources, cross-coupling and dissipation terms for the equations. Although the more general  $(-)$  averaging is used in the above notation, the only mean velocity component retained is  $v$ .

The pressure along the duct,  $\bar{p} = \langle p \rangle + p''(x,t)$ , is specified by the one-dimensional standing wave solution

$$p'' = \Pi_{ma} \langle p \rangle \cos(n\pi x/L) \cos(2\pi ft) \quad (7)$$

where  $\Pi_{ma}$  is the maximum relative acoustic pressure amplitude, and  $u_{ma} = \Pi_{ma} a_0 / \gamma$ . Steep-fronted waves are not considered in this investigation. All nonreactive flow calculations to be presented were performed at the velocity antinode of the first longitudinal mode. Material properties were those of air at standard conditions, or at elevated pressures where noted.

The turbulence length scale  $\Lambda$ , in this model is algebraic and described<sup>5</sup> by a linear variation from its surface value,  $\Lambda_s$  ( $\Lambda_s = 0$  for smooth walls), to a plateau level proportionate (with constant  $C_\Lambda$ ) to the thickness of the shear flow. For the present analysis this thickness was defined as  $\delta_{aa}$ , equal to the height above the surface where the boundary asymptotes to 99% of  $u''_c$ . For injected flows, however, waves are convected away from the surface. In these cases the first zero-crossing of  $u''$  was taken as the effective  $\delta_{aa}$ . The final values of  $\delta_{aa}$  used in the length scale expression were smoothed by integrating in time. An alternative differential length-scale equation would be more desirable, assuming that problems with the low turbulent Reynolds number behavior of such equations could be circumvented.

Boundary conditions at the duct centerline (or centerplane) are the symmetry conditions, which for the posed system are

$$\frac{\partial}{\partial r} [\bar{u}, \bar{h}, \overline{u'u'}, \overline{v'v'}, \overline{w'w'}, \overline{h'h'}, \overline{h'u'}] = 0 = \overline{u'v'} = \overline{h'v'}$$

Due to the final form of the governing equations, the requirement that  $\bar{v} = 0$  on the centerline (centerplane) is necessarily relaxed. At the duct surface, the static enthalpy corresponding to a given temperature is specified, and the mean injection velocity  $\bar{v}_s$  is prescribed. The no-slip condition implies that all tangential velocity components and their correlations are zero. Experiments have confirmed that strong injection rates through a porous plate can produce pseudo-turbulent disturbances which must be included in the ensemble average of the  $\overline{v'v'}$  boundary condition. The parameter  $\sigma_v^2 = \overline{v'v'}/\bar{v}^2$  was introduced in Ref. 5 to account for this important source of disturbance. All enthalpy correlations are null due to the prescribed uniform surface enthalpy.

## Gas-Phase Combustion Modeling

The gas phase equation for the ensemble mean enthalpy, under the assumptions outlined in the previous sections, is then

$$\begin{aligned} \bar{\rho} \frac{\partial \bar{h}}{\partial t} + (\bar{\rho} \bar{v} + \overline{\rho' v'}) \frac{\partial \bar{h}}{\partial r} + \frac{1}{r^v} \frac{\partial}{\partial r} (r^v \bar{\rho} \bar{h' v'}) \\ = \frac{1}{r^v} \frac{\partial}{\partial r} \left( r^v \frac{\bar{k}}{c_p} \frac{\partial \bar{h}}{\partial r} \right) + \frac{\partial \bar{p}}{\partial t} \\ + \mu \left[ \left( \frac{\partial \bar{u}}{\partial r} \right)^2 + (A + B \cdot \text{Re}) \frac{q^2}{\Lambda^2} \right] + \Delta h_g \bar{\omega} \end{aligned}$$

where  $\Delta h_g \bar{\omega}$  is the energy source term due to a single-step gas reaction, and A and B are constant parameters used in the turbulence model<sup>5,24</sup>. For the present analysis it has also been assumed that the Lewis number is unity, and that combustion of a homogeneous propellant occurs in a low Mach number region. The turbulent enthalpy correlations *above* the flame zone are necessarily neglected to avoid contragradiant diffusion which can result in numerical instability. The species mass fractions are expressed in terms of enthalpy, due to Zeldovich similarity<sup>24</sup>, even though the  $\partial \bar{p} / \partial t$  term in the enthalpy equation is retained. This assumption is based on an order of magnitude analysis of the unsteady mean enthalpy equation, valid in the flame zone, which yields the following condition for similarity:

$$\Pi \ll \frac{\rho c (\bar{v}_s)^2 (c_p)^2}{f R k_r}$$

The above expression shows that the relative importance of the  $\partial \bar{p} / \partial t$  term in the flame zone is dependent upon the pressure ratio of the oscillation and its frequency in addition to the common parameters associated with quantifying the characteristics of the flame zone. Since the above expression is satisfied for the example calculations to be discussed, the species mass fractions needed to evaluate

needed to evaluate the reaction rate expression are expressible in terms of enthalpy using the similarity approach and the expression for  $\omega$  is then

$$\omega = B_g T^{\beta_g} \exp(-T_{A_g}/T) \left[ \frac{\rho (H_e - H)}{\Delta h_g} \right]^\Phi$$

where,

$$\Delta h_g = \sum_{\alpha} (Y_{\alpha^*} - Y_{\alpha e}) h_{\alpha}^o$$

In the present analysis,  $\bar{\omega} = \bar{\omega}(\bar{T}, \bar{p})$  since it has been shown that the effects of near-surface turbulent reaction rate correlations are small for homogeneous propellants<sup>25</sup>.

### Unsteady Heat Conduction in the Condensed Phase

The unsteady condensed-phase heat conduction is determined through a coupled numerical solution of the gaseous and condensed phases employing an iterative procedure based on the gas/solid interface energy balance. The condensed-phase coordinate,  $\eta$ , runs from zero at the gas/solid interface to  $-\infty$  in depth. The gas-phase coordinate,  $y$ , runs from zero at the gas/solid interface to  $+\infty$  on the scale of the thermal boundary layer. The assumptions concerning the condensed phase are summarized for convenience in Appendix A. The condensed phase heat conduction equation, in the absence of subsurface reactions, is:

$$\frac{\partial T}{\partial t} + \dot{r} \frac{\partial T}{\partial \eta} = \alpha_{\pi} \frac{\partial^2 T}{\partial \eta^2} \quad (8)$$

An energy balance at the gas/solid interface yields the boundary condition at  $\eta = 0$ :

$$k_g \left. \frac{\partial T}{\partial y} \right|_s - k_{\pi} \left. \frac{\partial T}{\partial \eta} \right|_s = \rho_{\pi} \dot{r} [T_s (c_p - c_{\pi}) + l_s^o] \quad (9)$$

where the enthalpy of decomposition is



$$L_S^0 \equiv \sum_{\alpha} (h_{\alpha}^0)_g - h_{\pi}^0$$

In equation (9), the assumption of large chamber radius is made for convenience. Equations (8) and (9) are both nonlinear due to the fact that the surface regression rate,  $\dot{r}$ , is a strong function of the surface temperature,  $T_s$ . The regression (burning) rate, determined by condensed-phase sublimation or evaporation, is assumed to be governed by an Arrhenius pyrolysis law of the form:

$$\dot{m} = \bar{\rho}_s \bar{v}_s = \rho_{\pi} \dot{r} = A_s e^{-T_{As}/T_s} \quad (10)$$

Finally, the in-depth boundary condition is simply:

$$\eta \rightarrow -\infty, T \rightarrow T_{\pi} \quad (11)$$

where  $T_{\pi}$  is the constant in-depth propellant temperature.

Equations (8) through (11) completely specify the unsteady conduction of heat into the condensed-phase. The solution is obtained by performing a linear coordinate transformation on equations (8) and (9) to map the condensed phase onto the computational gas phase grid. Equation (8) and the gas-phase equations (6) are then solved numerically, using the Crank-Nicolson finite-difference method, and equation (9) is used to iteratively solve for the interface temperature. The linear transformation from  $\eta$ -space to  $y$ -space is:

$$y = \frac{1}{\zeta_{\pi}} \eta \quad (12)$$

where  $\zeta_{\pi} = k_{\pi} c_p / (k(T_s) c_{\pi})$  is a scaling parameter used to approximately match the depth of the combustion wave in the condensed-phase to the flame height in the gas phase. This transformation enables the condensed-phase solution to take full advantage of the dynamically adaptive gas phase grid and ensures consistent numerical treatment. Applying the transformation to equations (8), (9), and (11) produces the following system of equations

$$\frac{\partial T}{\partial t} - \frac{\dot{r}}{\zeta_{\pi}} \frac{\partial T}{\partial y} = \frac{\alpha_{\pi}}{\zeta_{\pi}^2} \frac{\partial^2 T}{\partial y^2} \quad (13a)$$

$$k_g \left( \frac{\partial T}{\partial y} \right)_{s,g} + \frac{k_{\pi}}{\zeta_{\pi}} \left( \frac{\partial T}{\partial y} \right)_{s,\pi} = \rho_{\pi} \dot{r} [T_s (c_p - c_{\pi}) + L_s^0] \quad (13b)$$

$$y \rightarrow +\infty, T \rightarrow T_{\pi} \quad (13c)$$

### Numerical Coupling of Condensed and Gas Phase Solutions

The gas/solid interface energy balance, Equation (13b), and the pyrolysis relation, Equation (10) provide the coupling between the condensed and gas phase solutions. The coupled solution is obtained by an iteration process (here referred to as a substep) at the new time step as follows:

- 1) Condensed and gas-phase solutions are obtained using the values of the gas/solid interface temperature and mean injection velocity specified at the previous temporal step or substep.
- 2) An updated interface mass flux is specified using Equation (13b) is obtained from:

$$\begin{aligned} (\dot{m}_s)_{n+1} &= (\rho_{\pi} \dot{r})_{n+1} \\ &= \left\{ \left[ k_g \left( \frac{\partial T}{\partial y} \right)_{s,g} + \frac{k_{\pi}}{\zeta_{\pi}} \left( \frac{\partial T}{\partial y} \right)_{s,\pi} \right] [T_s (c_p - c_{\pi}) + L_s^0]^{-1} \right\}_n \end{aligned}$$

where  $n$  and  $n+1$  are the  $n^{\text{th}}$  and  $n+1^{\text{st}}$  substeps, respectively.

- 3) equation (10) is inverted to obtain the corresponding surface temperature

$$(T_s)_{n+1}^i = -T_{As} / \ln \left( \frac{(\dot{m}_s)_{n+1}}{A_s} \right)$$

and the updated gas phase injection velocity is determined from

$$(\bar{v}_s)_{n+1} = (\dot{m}_s)_{n+1} / (\rho_g)_s$$

- 4) the condensed and gas phases are solved once again, using the updated values, and the process is repeated until convergence is achieved (typically in two or three iterations).

## RESULTS AND DISCUSSION

### STABILITY OF ISOTHERMAL ACOUSTIC BOUNDARY LAYERS

The initial profile for the axial velocity component was taken to be the analytical solution (at  $t = 0$ ) of Searl and Uchida (in Schlichting<sup>25</sup>) for oscillatory flow in a cylindrical duct. Initial profiles of the normal Reynolds stresses were taken to be isotropic, and proportional to the square of the initial velocity profile. The peak initial disturbance level,  $q_{\max}(t = 0, y)/u_{\max}$ , was assumed to be 0.01 for all calculations reported here.

The implicit numerical procedure and adaptive grid are described in prior studies<sup>5</sup>. Except where noted, approximately 50 time steps per period were employed. The number of radial spatial nodes within the boundary layer varied from about 40 for laminar flows to about 75 for turbulent cases.

Normalized profiles of the axial velocity in the laminar acoustic boundary layer ( $f = 1000$  Hz,  $\delta_a = 180$   $\mu\text{m}$ ) are shown for various times within a period in Figure 3. The results display the classical phase shift and Richardson annular effects due to viscosity. These calculations were performed with 100 time steps per period and produce a relatively small computational error, principally outside the boundary layer and near the maxima in the acoustic velocity. However, since a large number of calculations were needed for the transition studies, the number of time steps per period was halved for those calculations, and the error in the calculated acoustic velocity was then approximately doubled.

Figure 4 shows the axial velocity profiles for a fully (cyclically) turbulent boundary layer at 100 Hz with  $II_{\max} = .125$ . There is a noticeable diffusion of the Richardson effect and a pronounced increase in the velocity gradient near the surface. However, a protracted law-of-the-wall (logarithmic) region is not observed.

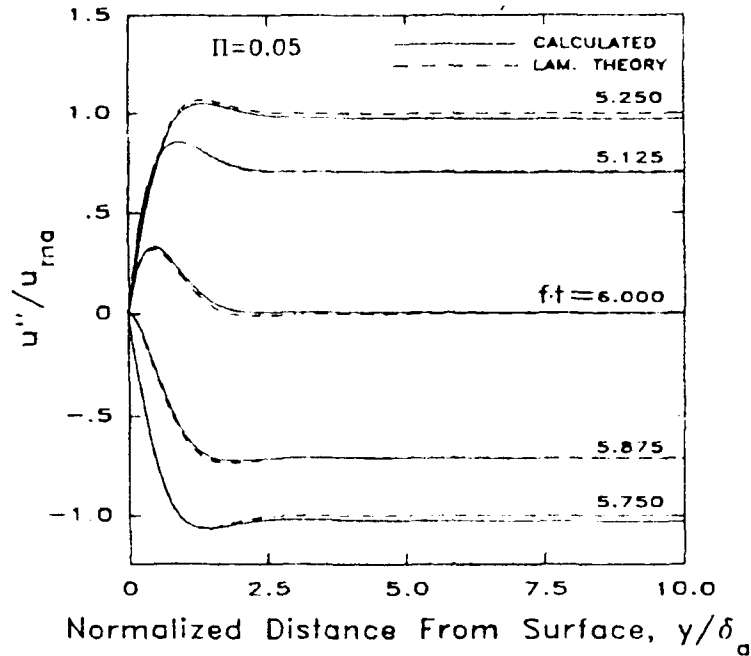


**Figure 3. Laminar velocity profiles in the acoustic boundary layer without injection.**

Figure 5 shows normalized turbulence intensity profiles,  $q/u_{ma}$ , in the boundary layer for the same conditions stated for Figure 4. The calculated peaks in turbulence level are comparable to those calculated for steady state flows ( $\approx 15\%$ ). To within computational accuracy, these peaks are symmetric with respect to  $\pm\pi ft$ . A slight phase lag, on the order of 5-10 degrees, exists between the intensity maxima and the rectified acoustic velocity  $|u''_c|$ . This lag increases at higher frequencies. Also note that the intensity decreases substantially, but is not predicted to vanish at the zero-crossings of  $u''_c$ .

Figure 6 shows turbulent velocity profiles for a Stokes layer with injection at  $f = 100$  Hz,  $\Pi = 0.080$ , and mean injection velocity  $\langle v \rangle = 1$  m/s. A pronounced Richardson effect is evident, surpassing even the laminar noninjected results. The estimated value of the effective boundary layer thickness for this case is 5.5 mm (approximately  $y/\delta_a = 14$  in the figure). The convective wave-train behavior shown is also evident in the laminar injected Stokes layer calculations of Glick and Renie<sup>7</sup>.

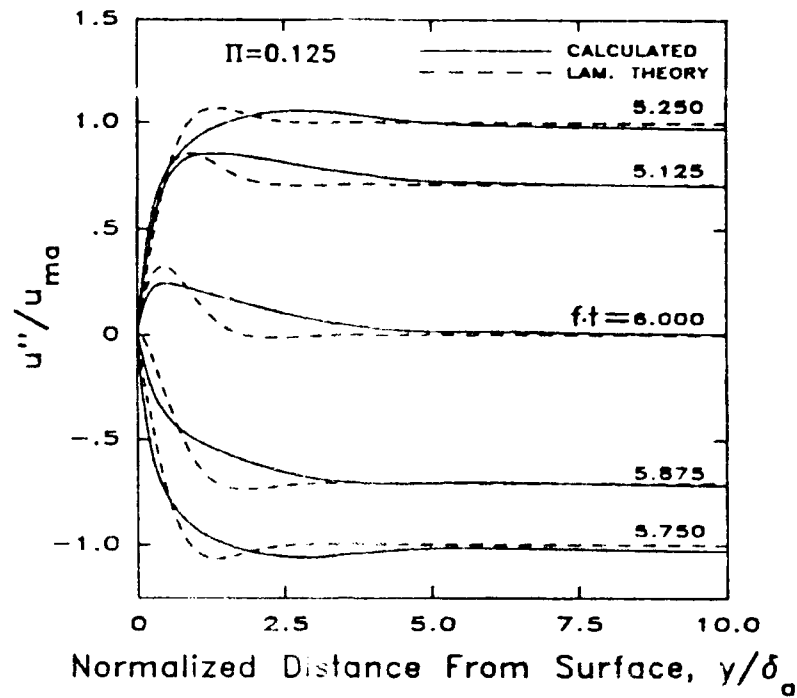


Figure 4. Turbulent velocity profiles in the acoustic boundary layer without injection.

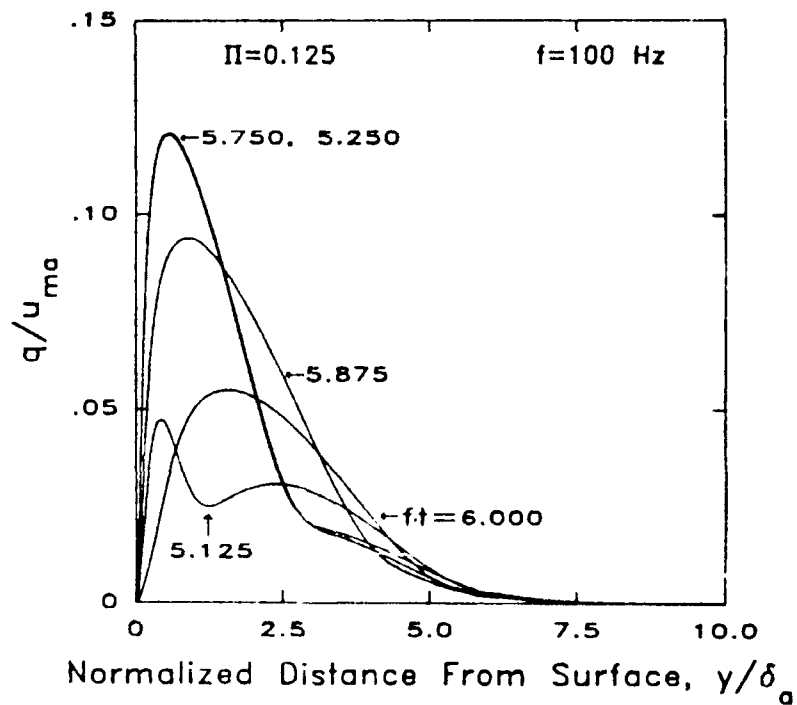


Figure 5. Turbulence intensity profiles in the acoustic boundary layer without injection.

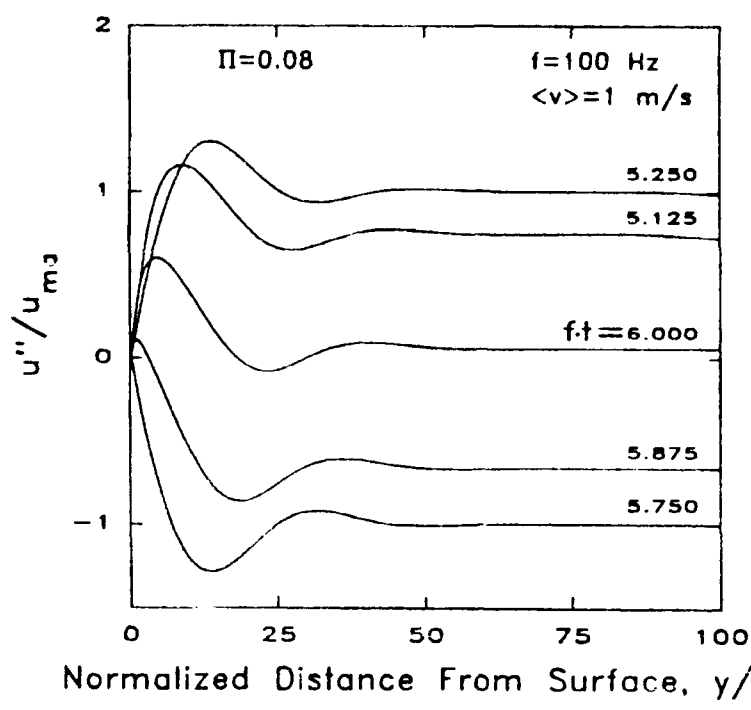


Figure 6. Turbulent velocity profiles in the acoustic boundary layer with injection.

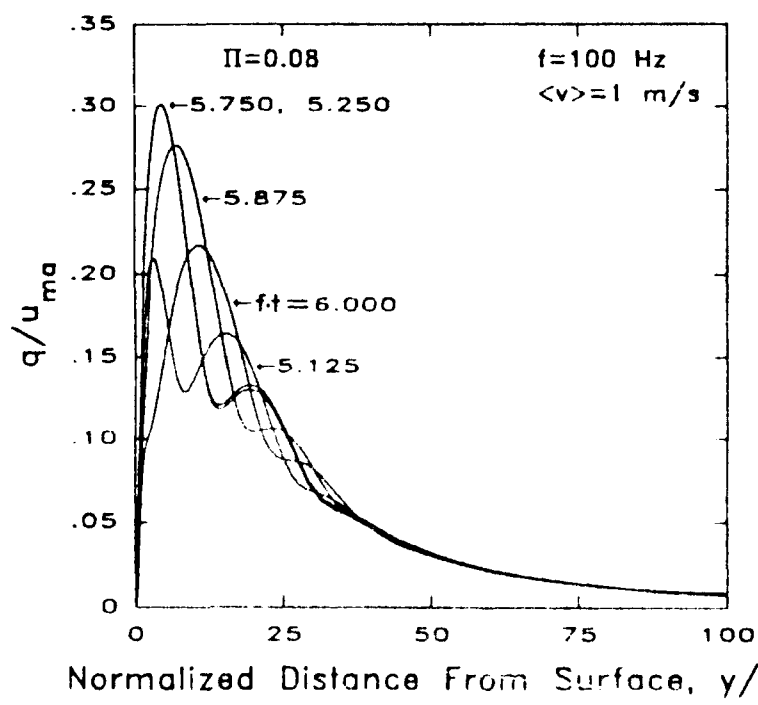


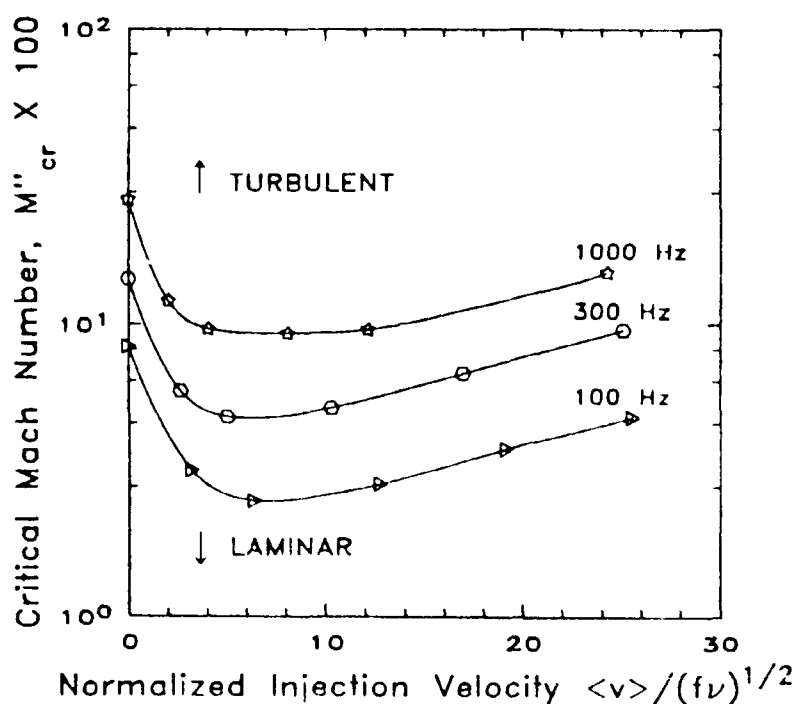
Figure 7. Turbulence intensity profiles in the acoustic boundary layer with injection.

Figure 7 shows the corresponding normalized turbulence intensity profiles. Due, in part, to the enhanced Richardson effect, very large intensity levels ( $\approx 30\%$ ) are predicted. As turbulence is produced in the inner layer at a later time in the cycle, the velocity wave formed from an earlier cycle produces a harmonic wave in the intensity profile ( $ft = 5.125$ ). A long tail is predicted due to large decay times and the fact that turbulence is beginning to accumulate at the computational centerline ( $\delta = 5$  cm) where the symmetry condition is employed. In an actual duct flow environment, the mean axial flow would convect these tails downstream as they interact with mean flow induced turbulence.

Calculated results for the critical acoustic Mach number at transition,  $M''_{cr} = \Pi_{cr}/\gamma$ , are shown in Figure 2 together with the approximate relation and data for non-injected Stokes layers. The functional dependence is similar, but the proximity of the calculations to the  $K = 750$  line is coincidental. Note, for example, that although not shown here, the numerical results display a dependence on the initial amplitude of turbulence assumed. "Transition" in the calculated results was determined by monitoring the growth or decay of initial turbulence from the initial value over several cycles. For the cases with injection, the growth rates were not as strongly dependent on as were those for the non-injected cases.

Critical Mach numbers for transition as a function of the normalized mean injection velocity,  $\langle v \rangle / (fv)^{1/2}$ , are shown in Figure 8 for three frequencies,  $f = 100$ , 300 and 1000 Hz. A pronounced *decrease* in  $M''_{cr}$  is predicted with increasing injection velocity, so that all curves exhibit a minimum that is frequency dependent. The minima are almost a factor of three below the  $M''_{cr}$  for noninjected Stokes layers. As an example, the 100 Hz non-injected Stokes layer is calculated to have  $M''_{cr} = .083$ . For the injected Stokes layer, the minimum value of  $M''_{cr} = .025$  occurs at  $\langle v \rangle \approx 0.25$  m/s, while  $M''_{cr} = .048$  at  $\langle v \rangle = 1.0$  m/s (the termination of the line at this frequency).





**Figure 8. Effect of injection on the stability of the acoustic boundary layer.**

Even more informative are the same results for transition normalized not as a critical acoustic Mach number, but as a *critical acoustic Reynolds number*,  $u_{ma}/(f\nu)^{1/2}$ . In this case, all three curves for frequency in Figure 8 collapse onto a single line (to within computational precision), shown as the upper line in Figure 9. This figure also shows results for finite levels of the surface disturbance parameter  $\sigma_v = 0.035$  and  $0.07$  for two different transition criteria to be discussed. The accompanying value of  $\Lambda_s$  assumed in the calculations was  $3 \times 10^{-4}$  m. These values are viewed as realistic and perhaps conservative. It is not surprising that this finite disturbance effect, which continuously "feeds" the injected layer, is predicted to yield further reduction in critical acoustic Reynolds number, analogously to quasi-steady flows.<sup>5</sup> As a specific example, the minimum critical Mach number for the 100 Hz case at  $\langle v \rangle = .20$  m/s is decreased to approximately one percent for  $\sigma_v = 0.035$ .

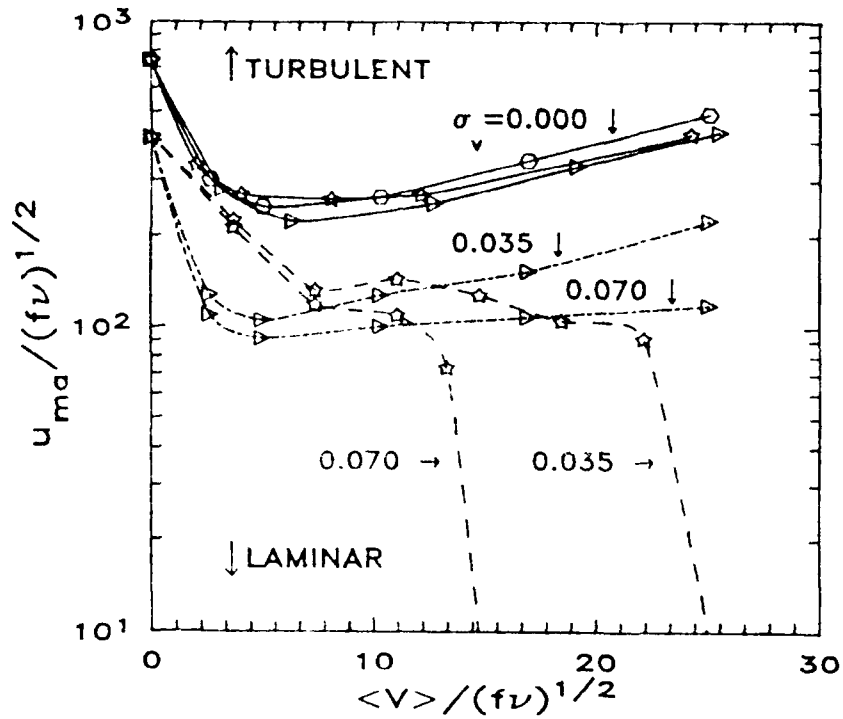


**Figure 9. Effects of injection and injection disturbance level on the stability of the acoustic boundary layer.**

As mentioned earlier, it was more difficult to determine the value of  $M''_{cr}$  for cases with injection and finite levels of  $\sigma_v$  present. The first criterion employed consisted of monitoring the maximum turbulence level  $q_{max}/u_{ma}$  occurring at any height within the boundary layer. If this maximum attained a value of 0.07 or greater within 3 cycles, the flow was considered turbulent. Using this criterion, the  $\sigma_v = 0$  lines were computed along with the alternating-dashed lines for  $\sigma_v = 0.035$  and 0.07. While this criterion was satisfactory for  $\sigma_v = 0$  cases, it proved to be unsatisfactory for cases with finite levels of  $\sigma_v$ .

To illustrate this effect, Figure 10 shows the variation of turbulence intensity vs normalized time at  $y = \delta_a$ , for three values of  $\Pi$ ,  $\langle v \rangle = 0.25$  m/s and  $\sigma_v = 0$ . It is evident from the curves in Figs. 10a and 10b that a very small increase in  $\Pi$  is able to cause the flow to transition to a cyclically turbulent condition.

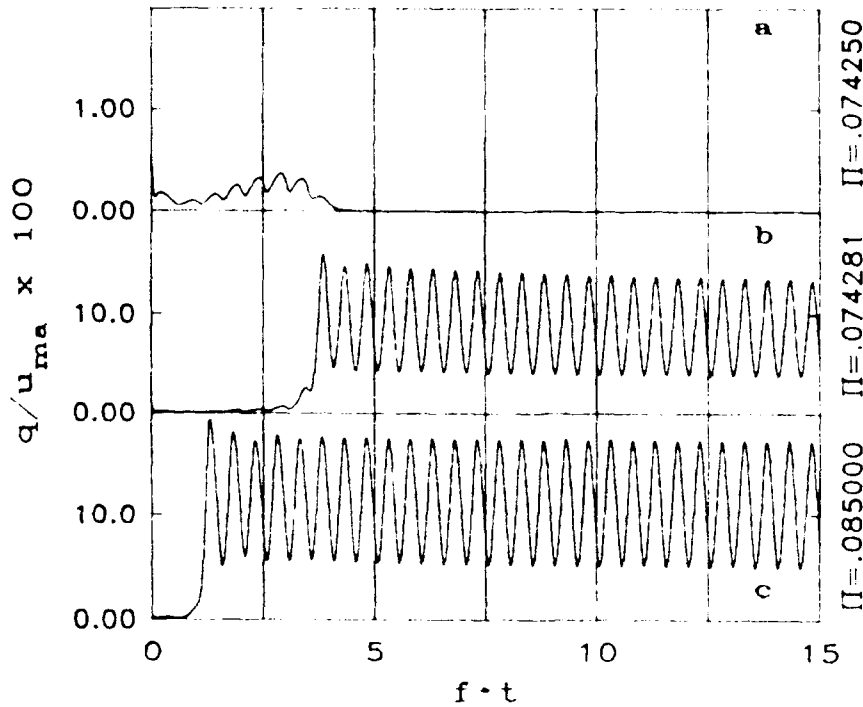


**Figure 10 (a-c). Time variation of turbulence development for the injected acoustic boundary layer ( $\sigma_v = 0$ ,  $y = \delta_a$ ).**

When finite levels of  $\sigma_v$  are included, the determination of  $\Pi_{cr}$  becomes more complicated. Figures 11a, b, and c are results for  $\langle v \rangle = 0.25$  m/s and  $\sigma_v = 0.035$ . Figure 11a is a case for which the turbulence bursts to a  $q/U_{ma}$  level of approximately 0.24 but then dissipates over 10 cycles until only the low level turbulence due to  $\sigma_v$  is still present. Figures 11b and c illustrate the increase in  $\Pi$  required to achieve the cyclic behavior which we considered to be characteristic of a turbulent case. This criterion for transition was used to calculate the dashed curves for 0.07 in Figure 9.

To recapitulate the results of the two transition criteria, the alternating dashed lines in Figure 9 qualitatively represent a "burst" or transient criterion for transition, while the dashed lines represent the particular (long-time) criterion. For the latter case, regions to the right of the nearly vertical line segments are indicated to be turbulent. The difference between the two criteria is in part explained by Equation (4), which must be augmented by the term  $\rho \langle v \rangle \frac{\partial q^2}{\partial y}$  when  $\sigma_v$  is finite. This can result in three different turbulence time scales being competitive under some conditions.

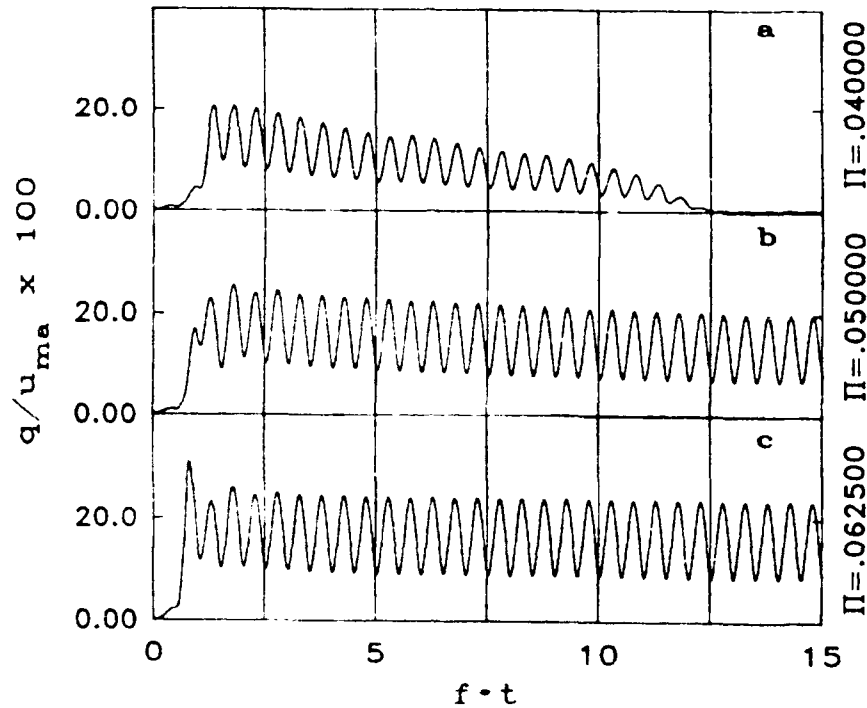


**Figure 11 (a-c). Time variation of turbulence development for the injected acoustic boundary layer ( $\sigma_v = 0.035$ ,  $y = \delta_a$ ).**

#### REACTIVE ACOUSTIC BOUNDARY LAYER - PRESSURE NODE

The thermochemical properties and reference operating conditions of the baseline solid propellant, presented in Appendix B, were chosen to represent the nominal properties of homogeneous propellants and were also used in the erosive-burning study of Ref. 26. Calculations presented were performed using the baseline propellant, which has an exothermic surface reaction ( $L_s^0 = -4.184 \times 10^5 \text{ J/kg}$ ), and an identical propellant with an endothermic surface reaction ( $L_s^0 = 837 \text{ J/kg}$ ). To reproduce the reference operating conditions, the pre-exponential constant in the gas phase reaction rate was calculated to be  $8.2 \times 10^9 \text{ kg}^{1-\Phi} \text{ m}^{\Phi-1} \text{ s}^{-1} \text{ K}^{\Phi} \text{ Bg}$  for the endothermic propellant. Steady-state calculations performed over a broad range of pressures yielded a normal rate of regression  $\dot{r} = \dot{r}^* (p/p^*)^n$  with  $\dot{r}^*$  and  $n$  as indicated in the Table. Transition calculations were performed using 50 time steps per cycle and two iterations per step while propellant response calculations were performed using 100 steps per cycle and three iterations per step. Unless stated otherwise, all propellant responses were obtained at an acoustic frequency of 1000 Hz and five

percent acoustic pressure ratio,  $\Pi_{ma} = 0.05$ . The disturbance level of the gas transpiring from the propellant surface,  $\sigma_v$ , was assumed to be zero in all calculations.

Shown in Figure 12 are the normalized steady-state temperature profiles obtained in the gas and condensed phases for the endothermic and exothermic propellant formulations at reference conditions, normalized by the approximate theoretical gas phase flame height,  $\delta_f$ , (note that the approximate  $\delta_f$  scaling used here is independent of  $L_s^0$ ). The results indicate that the exothermic formulation provides an anticipated increased gas phase flame height, increasing the possibility of acoustically induced turbulence interacting with the flame zone. The coincident condensed phase profiles are shown plotted in the gas phase computational coordinates and are therefore scaled by  $\zeta_\pi = 4.0$  in all calculations. Thus, if the scaling were not employed, the condensed phase combustion wave would be approximately four times the length of the flame zone and the condensed phase solution would not efficiently use the dense grid (generally 35 points) provided by the dynamically adaptive grid within the combustion zone.

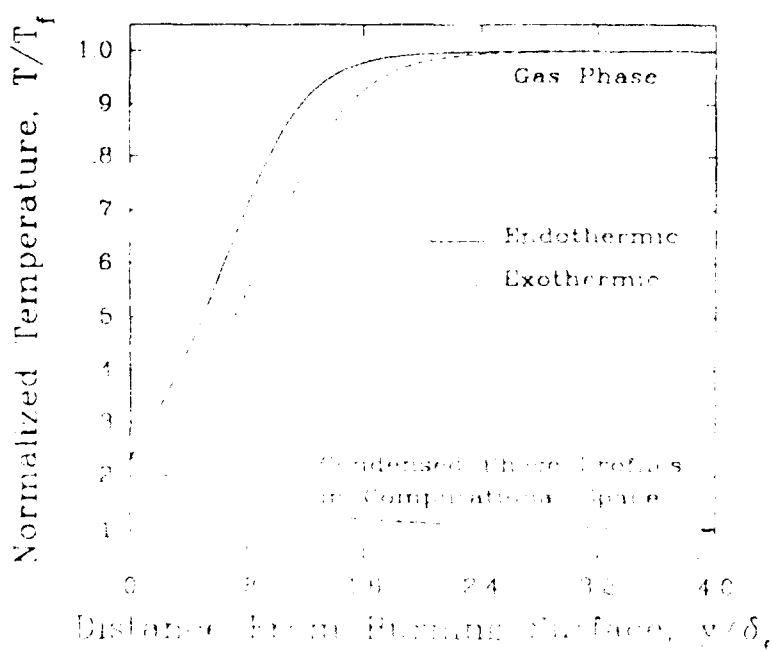
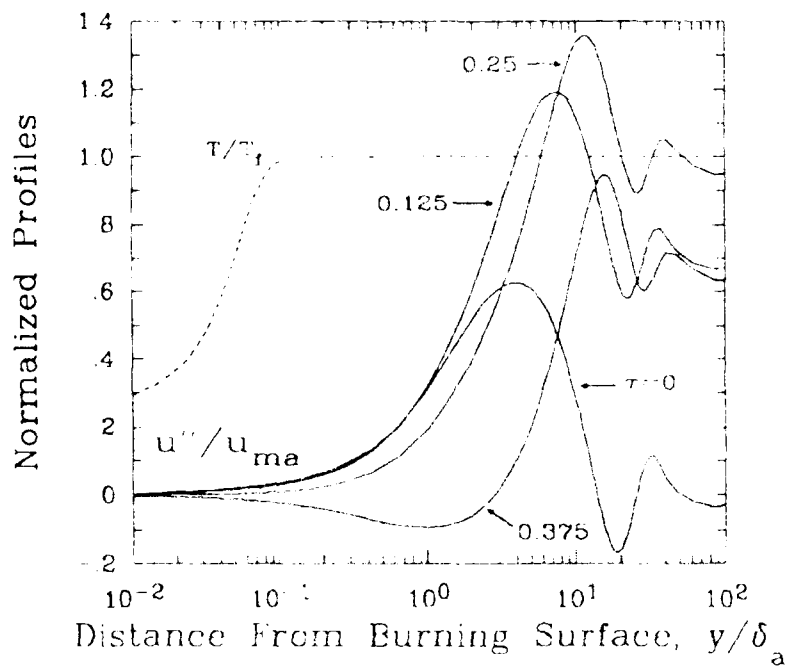


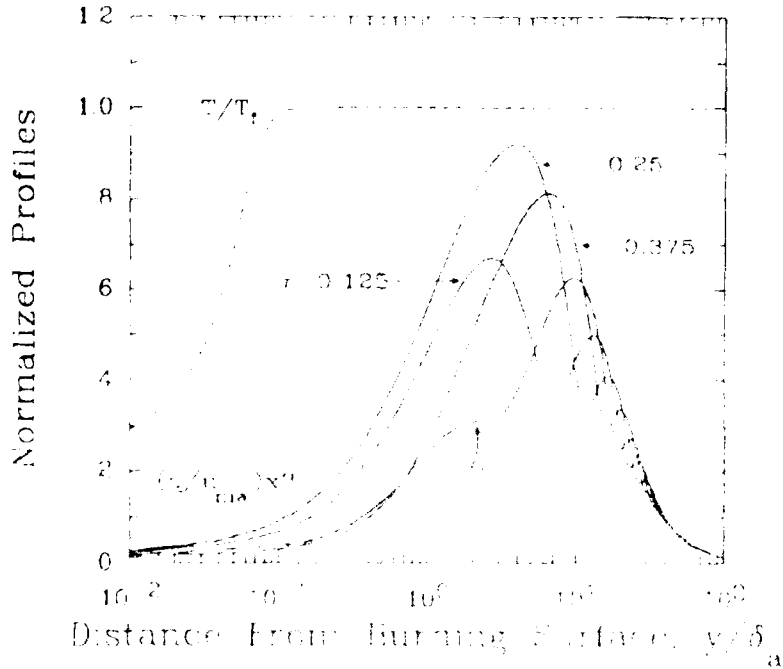
Figure 12. Steady state temperature profiles.

Figure 13 presents the normalized temperature and turbulent velocity profile vs. distance from the burning surface. The abscissa is normalized by  $\delta_a = 10 \text{ } \mu\text{m}$ . The profiles are given for various times within the acoustic cycle for the baseline propellant with an equivalent roughness of  $k_s = 150 \text{ } \mu\text{m}$ . The abscissa is presented as a logarithmic scale to reveal the details in the near surface flame region. The results obtained show the phase shift and Richardson annular effect due to viscosity and injection that were obtained in the previous section for isothermal Stokes layers. The acoustic velocity is negligible in the region of the flame zone at this intermediate frequency. Figure 14 shows the corresponding normalized temperature profiles and turbulence intensity profiles. The peaks in turbulence intensity within the cycle correspond approximately to the large velocity gradients produced by the Richardson annular effect. The results indicate that the turbulence intensity obtains magnitudes of one to two percent within the combustion region at certain points within the acoustic cycle, and results in propellant combustion responding to enhanced heating rates due to turbulent diffusion.

In a previous section, it was found that for a smooth surface ( $k_s = 0$ ) without surface injection disturbances ( $\sigma_v = 0$ ), an acoustic transition locus could be expressed in terms of axial acoustic velocity Reynolds number as a function of an injection velocity acoustic Reynolds number. Figure 15 shows the previously reported results. The critical amplitude locus is quite sensitive to the method used to introduce "seed" turbulence into the boundary layer and to other conditions such as the relative height within the boundary layer at which amplification is determined. Figure 15 shows additional calculations for an isothermal boundary-layer which utilize an alternative means of introducing the initial disturbance. (The difference between the two methods is that the earlier results introduced a 1% peak disturbance level within the Stokes layer thickness  $\delta_a$ , while the present results introduce the same 1% disturbance level over the much larger actual injected boundary layer thickness,  $\delta_{aa}$ ).



**Figure 13.** Comparison of temperature and turbulent velocity profiles at various times within a cycle.



**Figure 14.** Comparison of corresponding temperature and turbulence intensity profiles at various times within a cycle.

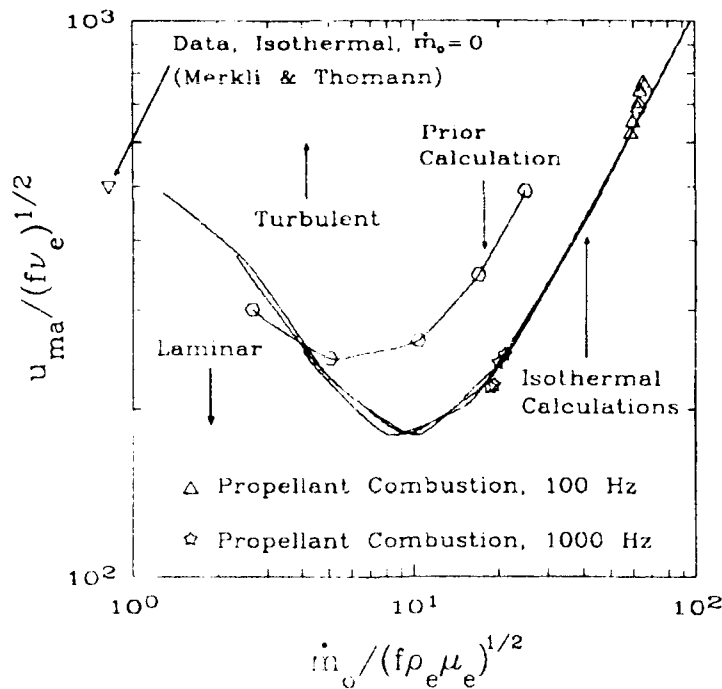


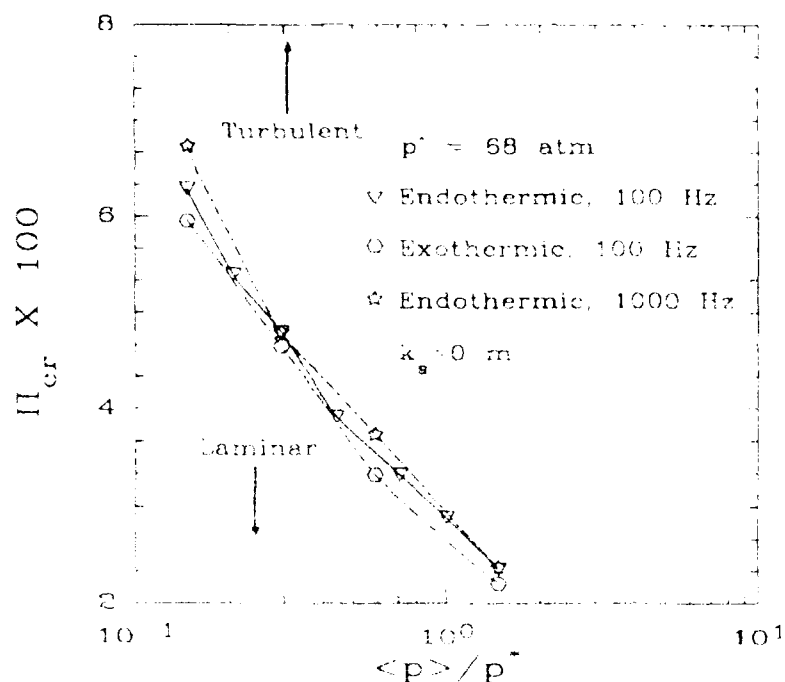
**Figure 15. Critical acoustic Reynolds number required for transition.**

Using this new and perhaps more realistic method, transition calculations were also performed for the baseline propellant at frequencies of 100 and 1000 Hz over pressures ranging from 10 to 100 atmospheres. The transition points obtained for propellant combustion are in good agreement with the isothermal calculations. Thus, the appropriate scaling involves flame or edge quantities only, and indicates that the acoustic flowfield (for a smooth surface) can be approximated as an isothermal flow at the steady-state flame temperature in determining transition.

Figure 16 shows the calculations presented in Fig 15, for the endothermic propellant along with calculations for the exothermic propellant at an acoustic frequency of 100 Hz, plotted as a function of the critical acoustic pressure ratio,  $\Pi_{cr}$ , vs. the mean pressure normalized by  $p^*$ . The critical pressure ratio is found to be insensitive to the heat released from the surface reaction, although the actual response of the propellant is dependent on  $L_s^0$ . This results from the fact that, for a smooth wall, transition is initiated above the thin combustion zone. The critical pressure ratio is found to decrease with increasing mean pressure in all cases, indicating that a propellant which may be stable with respect to a specific acoustic



node at a known mean pressure may encounter acoustic transition at that mode when operating at an elevated mean pressure. This phenomena may explain stability problems encountered in the development of solid rocket motors with unconventionally high chamber pressures.



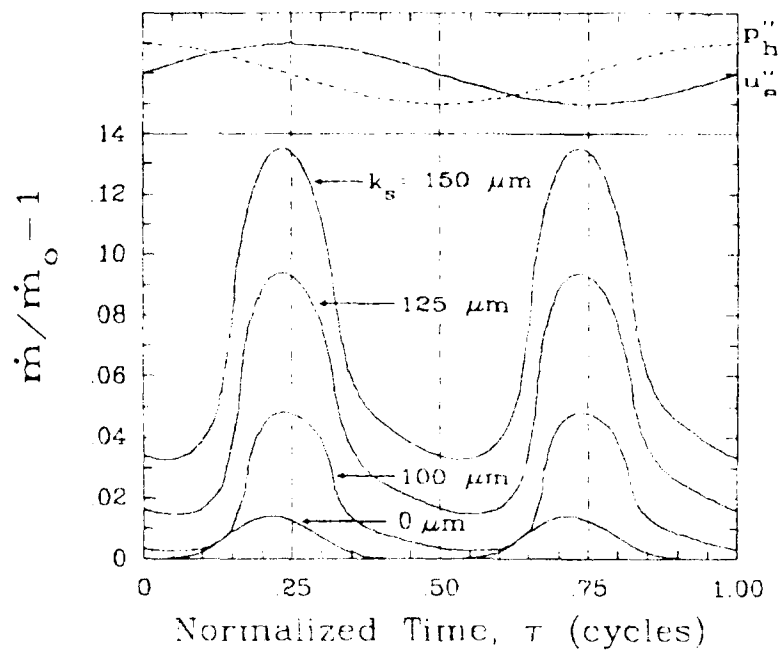
**Figure 16. Variation of critical pressure ratio required for transition as a function of mean chamber pressure.**

Figure 17 shows the response of the baseline endothermic propellant to the presence of the turbulent acoustic boundary-layer for various surface roughnesses. The normalized propellant mass flux (burn rate) is plotted vs. normalized time,  $\tau$ . A diagram of the variation of the acoustic edge velocity and pressure is included at the top of the figure. The pressure variation is correct for an axial location in the head-end region of a chamber. In the aft-end region, the pressure would be shifted 180 degrees in phase with respect to the pressure curve shown. The case of a smooth wall,  $k_s = 0$  m, required a 15 percent pressure ratio to obtain the response shown. The cases in which a finite value of surface roughness was prescribed were calculated using a five percent pressure ratio. The smooth wall produced only a slight response in the propellant burn rate that is rectified with respect to the velocity field and which is negligible over a large portion of each half cycle. The

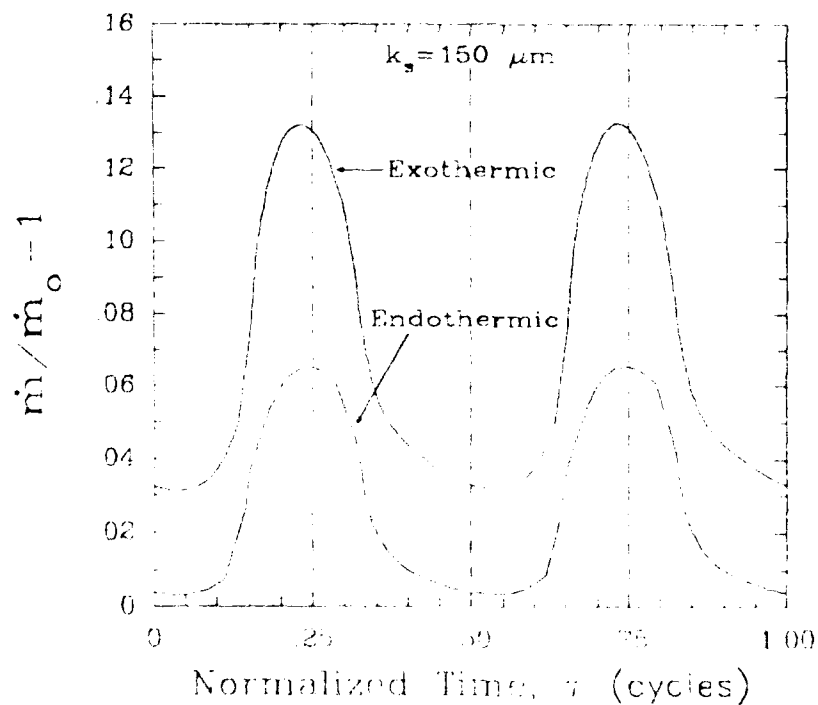
calculations in which finite levels of surface roughness are included reveal several interesting features. All cases exhibit the rectified response along with a time-mean augmentation ("D-C shift") of the propellant burn rate, about eight percent for  $k_s = 150\mu\text{m}$ , five percent for  $125\mu\text{m}$ , and two percent for the  $100\mu\text{m}$  surface roughness. The relative phase of the response, with respect to the acoustic velocity and pressure field, varies with surface roughness and may provide a mechanism by which the acoustical energy can be reinforced or damped.

Figure 18 compares the effect of surface decomposition energy on the propellant response. The calculations were performed for the endothermic and exothermic propellant formulations with  $k_s = 150\mu\text{m}$ , and  $\Pi = 0.05$ , in both cases. The exothermic propellant has a mean shift in burning rate that is approximately three times as large as that occurring in the endothermic case.

The propellant's response to the acoustic boundary layer is further investigated using a conventional Fast Fourier Transform (FFT) analysis over several cycles. The cases examined are identical to the calculations with finite roughness presented in Fig 17 and discussed above. Figures 19 and 20 present the results of the analysis in terms of the relative amplitude and frequency content of the response and the relative phase of the responses at each frequency, respectively. The large dashed curve is the driving frequency of the external acoustic velocity, the small dashed curve is the response of the propellant with a smooth wall (the response has been graphically shifted +300 Hz to facilitate the comparison), and the solid curve is the response with  $k_s = 150\mu\text{m}$ . The frequency content and relative amplitudes of the response with  $k_s = 150\mu\text{m}$  is representative of the cases with finite surface roughness. The results presented in Fig 19 have, in each case, been normalized by the largest amplitude obtained for that calculation after removal of the zero-frequency component. It can be seen that in both calculations the primary response occurs at the second harmonic with significant harmonic content occurring at the lower, even harmonics. Only even harmonics are obtained for this case since axial mean flow is neglected and calculations are performed at a pressure node. The relative phase of the propellant response, presented in Figure 20, is seen to vary substantially from harmonic to harmonic. It can further be seen that at the second harmonic, 2000 Hz, the phase lag of the response increases with increasing surface roughness (excluding the smooth wall case due to the large pressure ratio required to obtain the response).



**Figure 17.** Variation of propellant response as a function of time for various surface roughness heights.



**Figure 18.** Variation of propellant response as a function of time for endo- and exothermic surface decomposition energies.

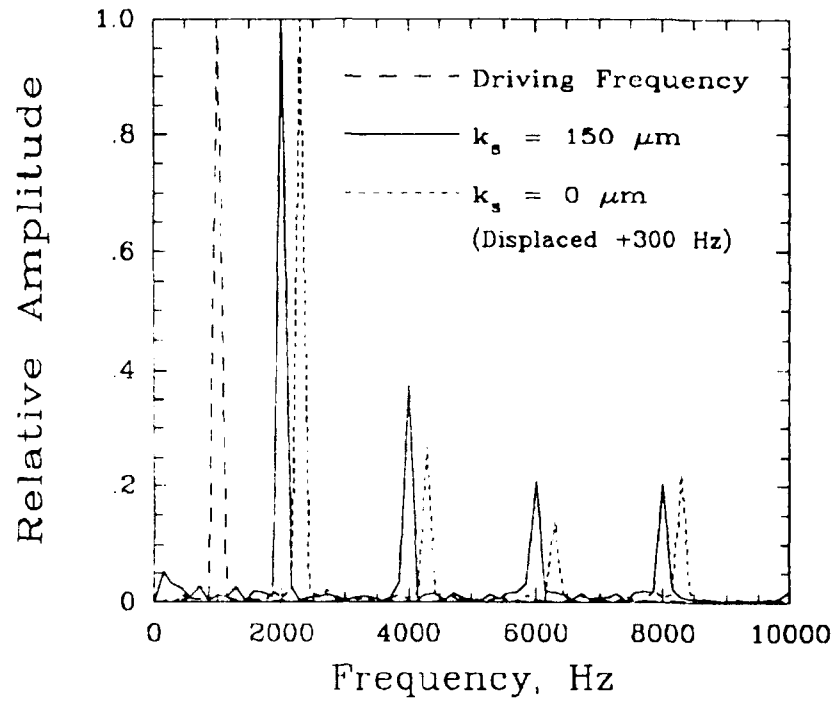


**Figure 19.** Harmonic content of the propellant responses shown in Figure 16 for a smooth and rough wall ( $k_s = 0$  and  $k_s = 150 \mu\text{m}$ , respectively)

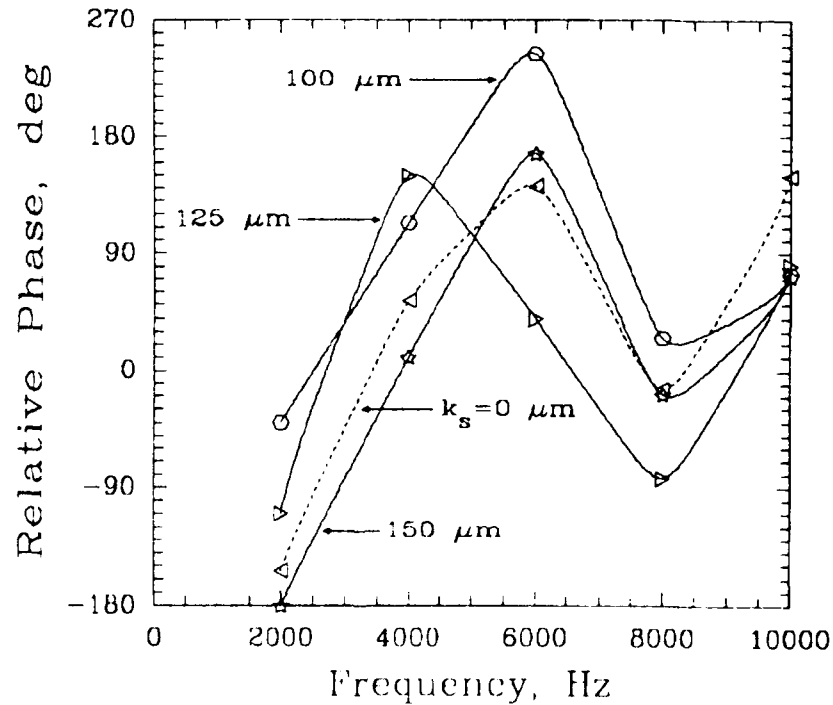


**Figure 20.** Relative phase angle of the responses shown in Figure 16.

## COMBINED RESPONSE AT VARIOUS AXIAL LOCATIONS

The thermophysical properties and reference operating conditions of the solid propellant employed in the previous section were also used to investigate the combined response and acoustic erosion at various axial locations. All calculations presented were performed using 100 time steps per cycle and three iterations per time step. When calculating the acoustic erosion of the propellant at various axial locations, the integration of the propellant response was performed in the 7th cycle of oscillation after the introduction of the seed turbulence in order to let the propellant combustion reach a cyclically steady-state. The integration required to calculate the acoustic erosion due to acoustic velocity oscillations alone were performed in the 3rd cycle of oscillation after the seed turbulence was first introduced since the flow would reach the cyclically steady-state condition in approximately two cycles. All calculations presented were performed at an acoustic frequency of 1000 Hz and five percent acoustic pressure ratio,  $\Pi_{ma} = 0.05$ , unless otherwise stated. The calculated acoustic boundary layer heights were  $\delta_{aa} \approx 1$  mm and 0.6 mm for an acoustic frequency of  $f=1000$  Hz and 2000 Hz, respectively.

The condensed-phase solution was calculated on the gas-phase computational grid after being scaled by  $\zeta_{\pi} = 4.0$  to use the dense grid provided by the combustion zone. The flame zone, which has a height of approximately  $10\mu\text{m}$ , generally had 35 grid points within it while the acoustic boundary-layer and remainder of the computational domain, which extends to a height of 5 cm, contained approximately 60 and 180 grid points, respectively. The disturbance level of the gas transpiring from the propellant surface,  $\sigma_v$ , was assumed to be zero in all calculations. The acoustic erosive burning is calculated by integrating the instantaneous propellant regression rate,  $\dot{r}$ , over one cycle of oscillation to obtain the long time mean of the regression rate,  $\langle \dot{r} \rangle$ , which is then normalized by the normal burning rate of the propellant,  $\dot{r}_n$ .

Shown in Figure 21 are the steady-state temperature profiles in the gas and condensed-phases normalized by the steady-state flame temperature,  $T_f$ , as a function of distance from the burning surface normalized by the approximate theoretical laminar flame height,  $\delta_f$ . The condensed-phase temperature profile is plotted in the gas-phase computational coordinates and has therefore been scaled by  $\zeta_{\pi} = 4.0$  as it is in all calculations. The calculated profiles are in good agreement

with the approximate theoretical flame height and theoretical condensed-phase thermal boundary-layer depth.

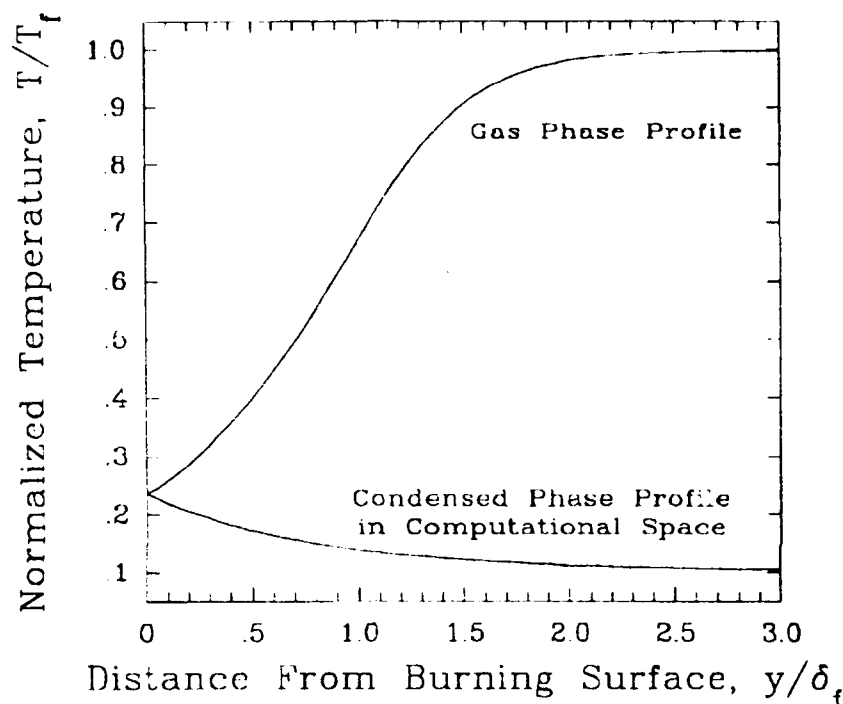


**Figure 21. Normalized steady-state temperature profiles.**

Figure 22 is a comparison of the gas-phase temperature perturbations due to acoustic pressure oscillations (laminar case) calculated both with and without the assumption of Zeldovich similarity. The latter case being equivalent to the equation system used in Tien's analysis.<sup>27</sup> The calculations were performed at  $x/L=0.375$  with  $\Pi_{ma}=0.05$  (which yields a local acoustic pressure ratio of 1.913 percent ( $\Pi_l=0.01913$ )) and are found to be virtually identical. The perturbations presented are defined, following the analysis of Ref. 27, as the difference between the instantaneous value and the steady-state value of the variable normalized by a reference condition (normally a value occurring at the edge of the flame zone) and the local acoustic pressure ratio. Various profiles throughout one cycle of oscillation are plotted as a function of normalized distance from the burning surface to a distance of 1000 theoretical flame heights. The perturbations qualitatively agree with the results of Ref. 27 and verify the oscillatory behavior of the wave train exterior to the flame zone. A direct comparison with the results of Ref. 27 was not

possible since thermochemical parameters of a representative solid propellant were selected for this study, whereas the nondimensional parameters of Ref. 27 produce inordinately low regression rates and/or high frequencies. This would imply that the (dimensional) frequencies required for a direct comparison with the results of Ref. 27 be the order of  $10^6$  Hz. At frequencies of this magnitude, many of the assumptions of both analyses would be invalid. Calculations up to  $10^4$  Hz were performed which appeared to be in qualitative agreement with the perturbation results of Ref. 27.

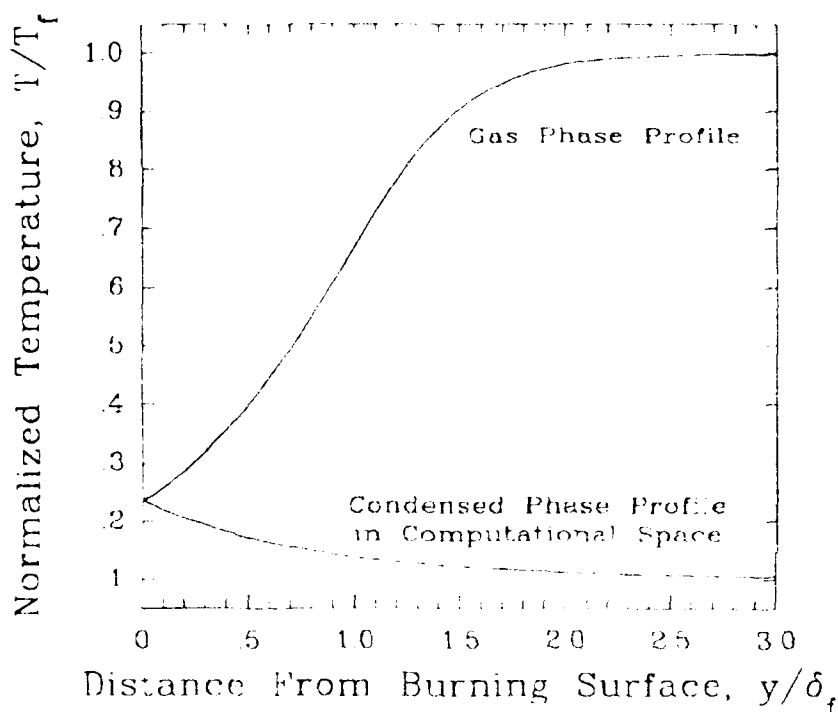


**Figure 22. Comparison of normalized temperature perturbations with and without the similarity assumption.**

The curves presented in Figure 23 are of the laminar and turbulent gas-phase temperature perturbations occurring at various points within one cycle of oscillation plotted as a function of normalized distance from the burning surface corresponding to the gas-phase flame zone plotted in Figure 21. The calculations were performed at  $x/L=0.375$ , with  $H_f=0.01913$  (the value of  $H$  at  $x/L$ ) and  $f=1000$  Hz. The low-amplitude, laminar-flow perturbations oscillate symmetrically about the steady-state solution, as expected. The turbulent perturbations are found to all

be positive, accounting for the increase of approximately 5 percent in the mean regression rate of the condensed-phase (DC-shift) at this location, and are substantially larger in magnitude than the corresponding laminar perturbations. It is noted that the "turbulent" perturbations presented are actually the combined response due to both turbulent flow and harmonic pressure fluctuations, but will be referred to as the "turbulent" perturbations in subsequent text for brevity.

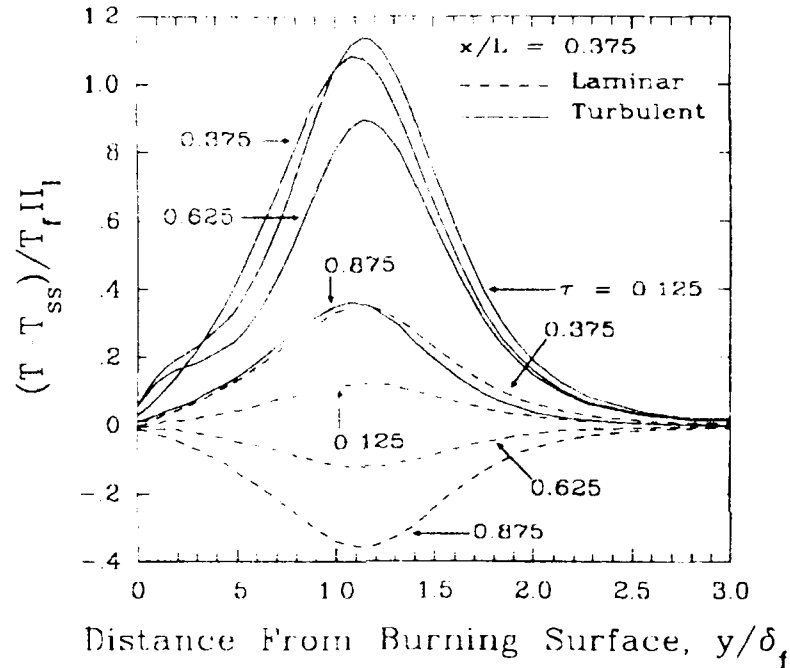


**Figure 23. Normalized laminar and turbulent gas-phase temperature perturbations.**

Figure 24 compares the laminar and turbulent gas phase normal velocity perturbations directly corresponding to the temperature perturbations presented in Figure 23. The laminar perturbations have been scaled in magnitude by a factor of 5 for presentation. It is evident that the pressure response is dominated by the effects of turbulence produced by the acoustic motion. The turbulent normal velocity perturbations at the surface and edge of the flame zone are found to oscillate about a mean shift corresponding to the shift in the regression rate of the condensed-phase.



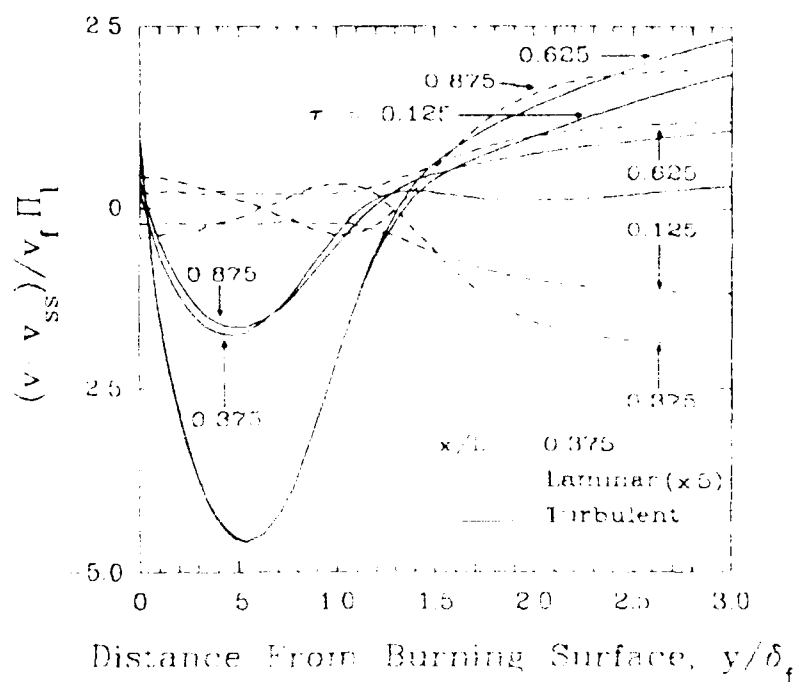


**Figure 24. Normalized laminar and turbulent gas-phase normal velocity perturbations.**

The laminar and turbulent perturbations of the condensed-phase temperature, directly corresponding to the curves presented in Figs. 21, 23 and 24, and plotted in the gas-phase computational space are shown in Figure 25. The magnitude of the laminar perturbations have been scaled by a factor of 5 for presentation. The laminar perturbations do not oscillate about the steady-state profile, as the laminar gas-phase perturbations do, but oscillate about an asymmetrical mean perturbation. This asymmetry arises from the variation of the regression rate (and therefore, convection) of the condensed-phase throughout the cycle of oscillation in combination with the oscillatory nature of the temperature at the gas-solid interface. The turbulent perturbations are found to be on the order of ten times larger than the corresponding laminar perturbations. The extremely asymmetrical behavior of the turbulent profiles is due primarily to the increase in the mean regression rate of the condensed-phase at this location, which tends to reduce the depth of the thermal boundary layer. The laminar and turbulent acoustic velocity profiles and the corresponding turbulence intensity profiles are essentially identical to the corresponding figures of the previous section.

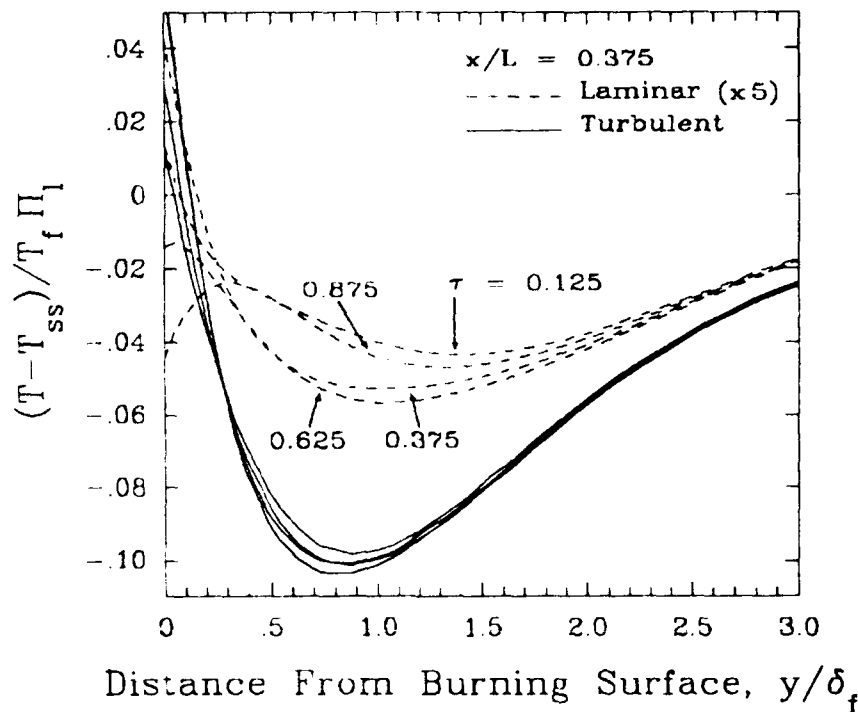


**Figure 25. Normalized laminar and turbulent condensed-phase temperature perturbations.**

Results have been obtained for the response of the propellant regression rate to conditions which would be representative of those existing in a center-vented T-burner, or in the head-end region of a solid rocket motor where the mean axial Mach number is low, when either are experiencing acoustic oscillations. For the fundamental mode, the acoustic environment varies from the pure pressure oscillation at either end to the pure velocity oscillations in the center of the chamber at the pressure node, and a combination of both at any point between. Only results for the portion of the duct from  $x/L=0$  to  $x/L=0.5$  will be presented since in the absence of a mean axial flow the response will be cyclically identical in either end of the duct.

The combined response of the condensed phase regression rate at various positions along the chamber are shown in Figure 26. The top portion of the plot contains a diagram of the corresponding acoustic pressure oscillation and the two possible external acoustic velocity oscillations which could exist at each location along the chamber (the diagram shows only the relative phases of, and is not intended to show the amplitude relationship between, the acoustic velocity and

pressure). The calculations were performed for  $\Pi_{ma} = 0.05$  and  $k_s = 150\mu m$ . The response of the condensed-phase regression rate at the end of the chamber,  $x/L=0$ , is sinusoidal and lags the pressure by approximately 9 degrees. At a quarter point in the duct,  $x/L=0.25$ , the turbulent acoustic boundary-layer produces a slight increase in the mean regression rate (1.8 percent) on which the sinusoidal response of the regression rate to the acoustic pressure is superimposed. As the location is moved closer to the center of the chamber, nearer the pressure node, the acoustically produced turbulence begins to dominate the dynamics of the combustion zone. At  $x/L=0.3125$  the sinusoidal behavior of the response has nearly vanished as the response becomes increasingly rectified. At  $x/L=0.4375$  the response is almost completely rectified due to the turbulence, yet the small acoustic pressure oscillation which exists produces discernable variations in the peaks and troughs of the response. At the pressure node,  $x/L=0.5$  (not shown), the response is completely rectified and has a mean shift of 6.6 percent, the maximum in the chamber.

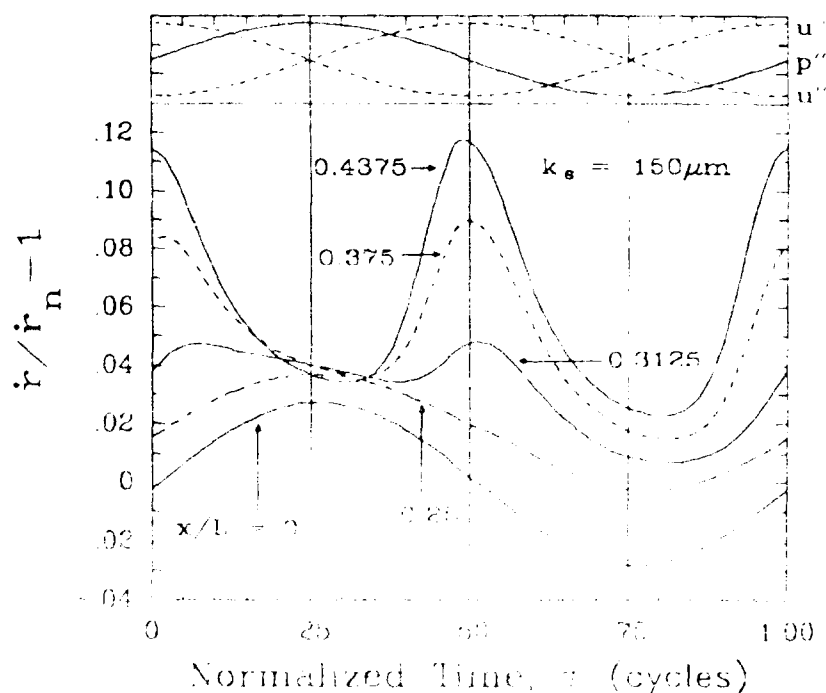


**Figure 26. Combined response of the condensed-phase regression rate as a function of axial location.**

The response of the condensed phase regression rate to the acoustic boundary layer is further investigated using a conventional Fast Fourier Transform (FFT)

analysis on 6 cycles of oscillation containing 600 points of data. The variation of the frequency content of the response along the axis of the chamber was calculated for  $f=1000$  Hz,  $\Pi_{ma}=0.05$ , and two equivalent sand roughness heights,  $k_s=150\mu\text{m}$  and  $k_s=100\mu\text{m}$ . Figure 27 shows the normalized frequency content for  $k_s=150\mu\text{m}$  at various locations along the duct and includes the responses plotted in Figure 26. The results presented at each axial location have, in each case, been normalized by the largest amplitude obtained in the entire chamber after removal of the zero frequency component corresponding to the DC-shift in the mean regression rate. The primary response from  $x/L=0$  to  $x/L=0.25$  is seen to be that of the driving frequency corresponding to the acoustic pressure oscillation. The lack of any harmonic content in this region is due to the nearly first order ( $\Phi=1.1$ ) gas-phase reaction. In the region from  $x/L=0.3125$  to the center of the chamber the frequency content is characterized by a steady decrease in the amplitude of the fundamental frequency and a rapid rise in the amplitude of the second harmonic corresponding to the rectified turbulent response. There is a similar appearance, and growth in the amplitudes of, the higher even harmonics along with the appearance of some very

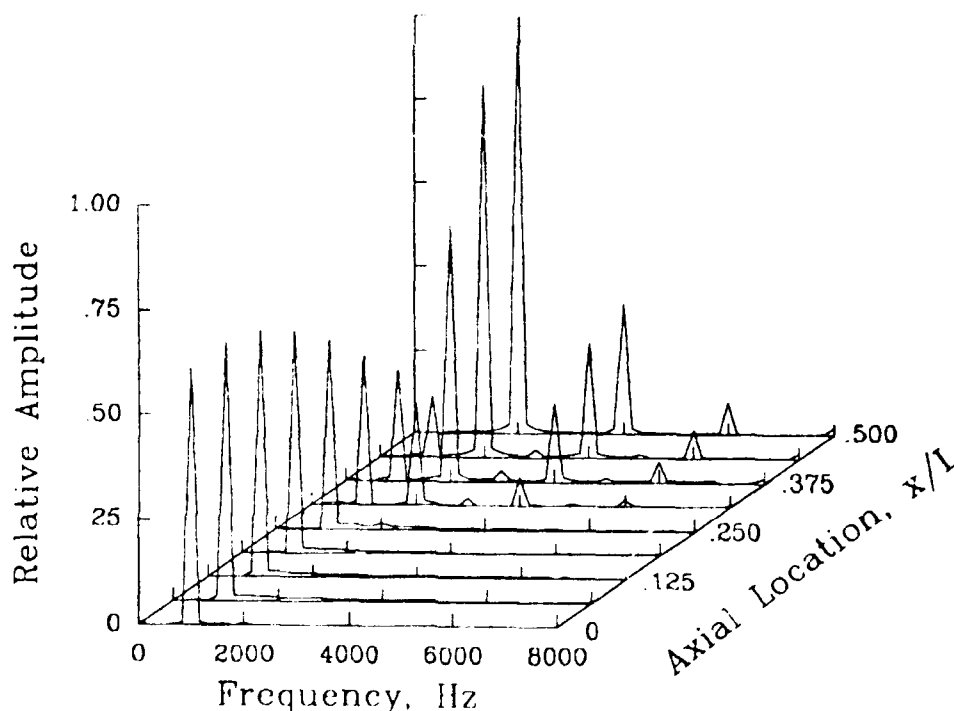


**Figure 27.** Harmonic content of the combined response versus axial location for  $\Pi_{ma} = 0.05$ ,  $f = 1000$  Hz, and  $k_s = 150\mu\text{m}$ .

small odd harmonics. The largest response is seen to occur at the center of the chamber due to the acoustically induced turbulence and is approximately double the amplitude of the largest pressure response, which occurs at  $x/L_c=0$ . Examining the frequency content at the center of the chamber reveals that only a completely rectified response with even harmonics is produced, as was shown in the previous section, by the turbulent acoustic velocity oscillations alone. It can be seen that, although no odd harmonics are produced by either the pure acoustic pressure or turbulent acoustic velocity oscillations alone, in combination they do produce detectable odd harmonics. The calculated FFT results corresponding to the 100 $\mu$ m equivalent sand roughness height were qualitatively identical to the results presented in Figure 27, differing only in the magnitude of the turbulent response.

The results presented in Figs. 26 and 27 may also be examined to assess whether the acoustic oscillations within the chamber could be damped or reinforced by the propellant response. The frequency response presented in Figure 27 indicates that an acoustic oscillation at the fundamental frequency is capable of introducing energy to acoustic modes at the higher harmonic frequencies. The response shown in Figure 26 indicates that the energy added over one cycle to the acoustic oscillations would be negligible towards the center of the chamber due to the nearly complete rectification of the combined response. The potential for combustion instability arising in an actual rocket chamber, due to the combined response, will depend upon the extent to which the turbulent component is biased, and shifted in phase, with respect to the local pressure oscillation by the interaction of the developing mean axial flow with the acoustic boundary-layer and turbulence fields. The relative magnitude of the turbulent and pressure components of the combined response indicate that the turbulent component could potentially contribute a larger portion of acoustic energy to the overall flowfield than that due to pressure coupling alone.

## COMPARISON OF ACOUSTIC AND STEADY-STATE EROSIVE BURNING

The experiments of Crump and Price<sup>15,17</sup> using center vented T-burners to investigate the combustion of solid propellants in an oscillatory environment, produced valuable data concerning the effects of acoustic erosion throughout the chambers of such devices. Ref. 15 presents data on the variation of acoustic erosion

throughout the length of the chamber of the T-burner. The results all exhibit a maximum increase in mean regression rate at the pressure node, corresponding to the maximum in acoustic oscillations, and a minimum in mean regression rate at each end of the chamber. They inferred that the reduction in regression rate below its normal value (often referred to as "negative erosion") was produced by a negative pressure response near each pressure antinode and a positive velocity response near the pressure node. The Soviet experimenters, Medvedev and Revyagin<sup>14</sup>, verified the results of Crump and Price with T-burner experiments of their own and suggested that the large increase in the mean regression rate may be due to the turbularization of the Stokes layer close to the surface of the burning propellant. Figure 28 shows the variation of the acoustic erosion as a function of axial location within the chamber for calculations with  $k_s=100\mu\text{m}$ ,  $125\mu\text{m}$ , and  $150\mu\text{m}$ . All of the calculations were performed at  $f=1000\text{ Hz}$  and  $\Pi_{ma}=0.05$ . An equivalent sand roughness height of  $150\mu\text{m}$  is found to produce an acoustic erosion of approximately 1 percent from very near the end of the chamber to  $x/L=0.3125$ , where the erosion begins to rise rapidly to a maximum of 6.6 percent at  $x/L=0.5$ . Values of  $100\mu\text{m}$  and  $125\mu\text{m}$  equivalent sand roughness heights produce similar variations of erosion throughout the chamber, differing substantially only in their respective magnitudes. The acoustic erosion remains zero to approximately  $x/L=0.25$  and then increases to the maximum values of 1.6 percent and 4 percent at  $x/L=0.5$ . The lack of negative erosion near the pressure antinodes in the present calculations may be a result of the choice of propellant thermophysical parameters or the simplifying assumptions made for the combustion process.

Figure 29 shows additional experimental results concerning erosive burning obtained by Crump and Price and Medvedev and Revyagin as presented in Ref. 14. The mean shift in the condensed phase regression rate is plotted as a function of the velocity,  $u_e$ , for both acoustic and steady-state erosive conditions. Here,  $u_e$  represents the centerline velocity of the steady-state experiments and the amplitude of the acoustic velocity oscillation in the oscillatory experiments. A different propellant was used by each set of experimenters, but the same trends were discerned. First, the acoustic erosion threshold velocity was found to be approximately half of the threshold velocity for steady-state erosion. Second, the acoustic erosion was noted to be approximately linearly related to the maximum amplitude of the acoustic velocity oscillation.

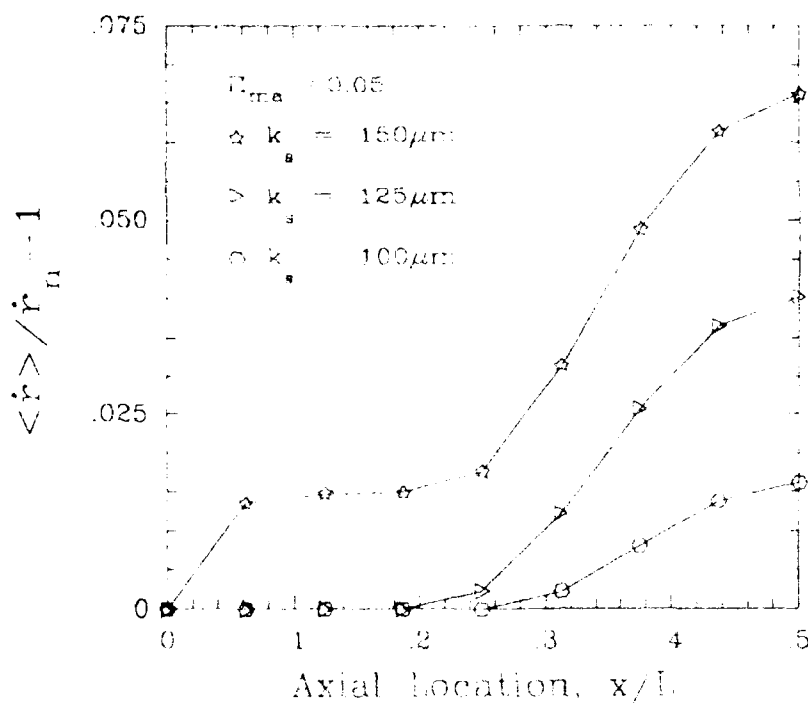


Figure 28. Acoustic erosion vs axial location within the chamber for various equivalent sand roughness heights.

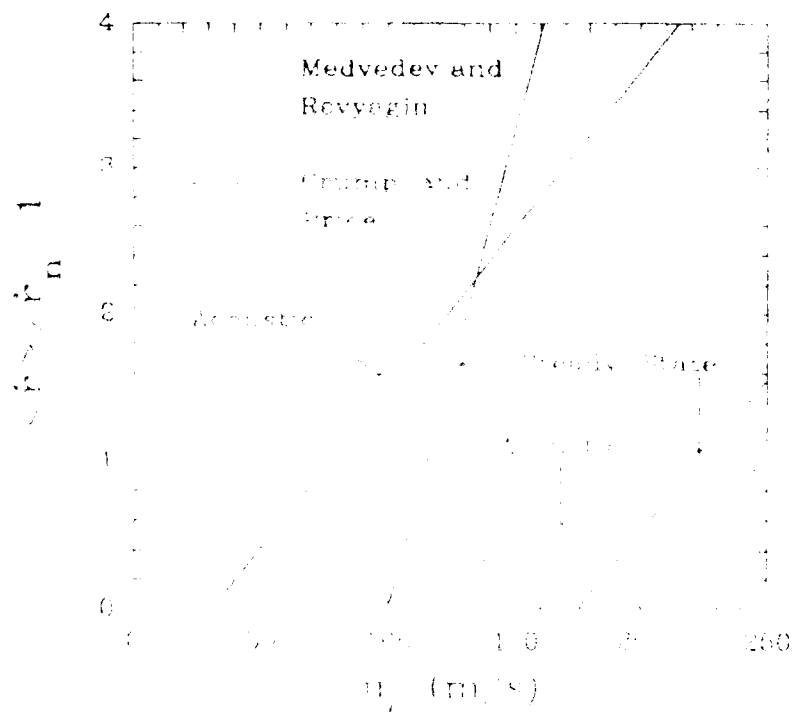


Figure 29. Experimental comparison of acoustic and steady-state erosion (after Ref. 11)

Figure 30 shows results of calculations of acoustic and steady-state erosion for the propellant considered in the present investigation, assuming two values of equivalent sand roughness height,  $k_s=150\mu\text{m}$  and  $100\mu\text{m}$ . The acoustic calculations were performed at the pressure node to insure that the response was due solely to the acoustically induced turbulence. The maximum acoustic velocity amplitude at which a calculation can be performed for is limited by the corresponding maximum allowable Reynolds number, based on wall shear stress and equivalent sand roughness height, above which the validity of the surface roughness model is questionable<sup>26</sup>. The steady-state calculations were performed using the SPEC<sup>24</sup> code at the same operating conditions, and for the same propellant formulation, as the acoustic calculations. The present calculations predict the acoustic threshold velocity to be less than half the threshold velocity of steady-state erosion and the acoustic response is seen to vary nearly linearly with velocity after the initial response appears. Both of these results agree well with the experimental results shown in Figure 29. It should be noted, however, that the calculated relative slopes of the acoustic and erosive burning curves do not correspond to the experimentally obtained results.

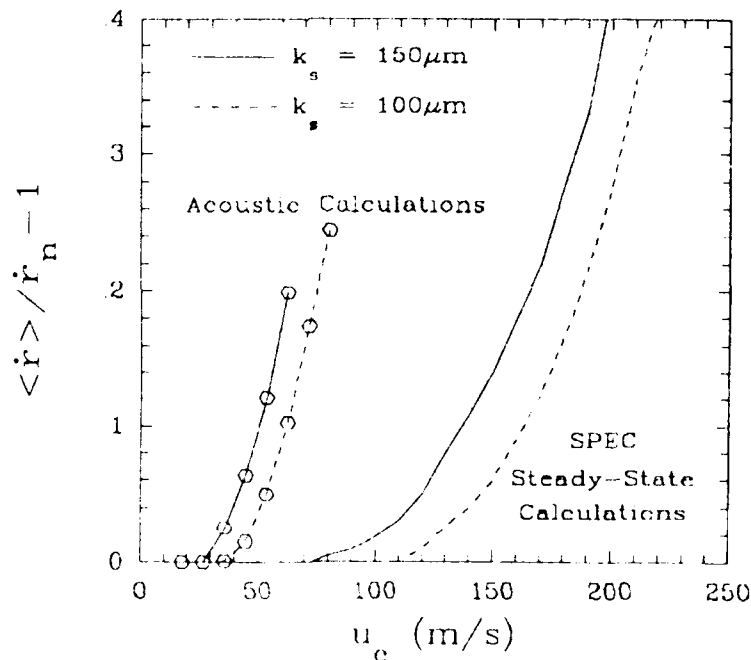
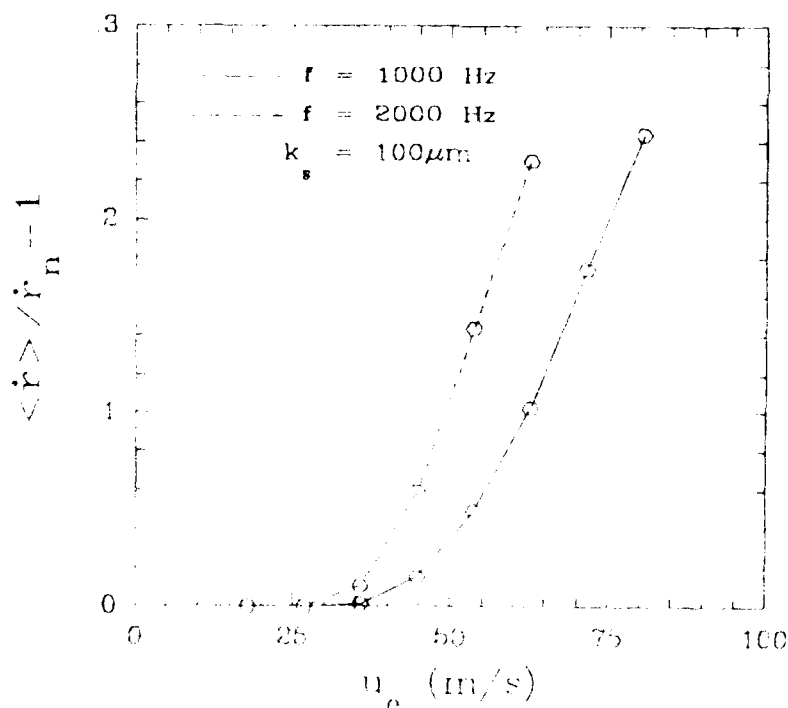


Figure 30. Comparison of calculated acoustic and steady-state erosion.



The ability of the acoustically induced turbulence to interact with the combustion process is directly related to the height of the acoustic boundary-layer,  $\delta_{aa}$ , which is inversely related to the frequency of the acoustic oscillations. Medvedev and Revyagin reported that the magnitude of the acoustic erosion was a weak function of acoustic frequency and suggested it may be due to the decrease in the height of the Stokes layer. Figure 31 shows the results of calculations performed to investigate the frequency dependence of the acoustic erosion for the present propellant combustion parameters. The calculations were performed at  $f=1000$  Hz and  $2000$  Hz with an equivalent sand roughness height of  $k_s=100\mu\text{m}$ . The frequency dependence is predicted to be quite strong for the propellant thermophysical parameters of this investigation. For example, at  $u_e=60$  m/s, the acoustic erosion is predicted to be approximately 9 percent at  $f=1000$  Hz and 21 percent at  $f=2000$  Hz.



**Figure 31.** Comparison of calculated acoustic erosion at acoustic oscillations of 1000 Hz and 2000 Hz.

## CONCLUSIONS

An analysis of transitional and turbulent acoustic boundary layers in the presence of strong injection has been presented. The problem was approached by analyzing the behavior of a second-order turbulence model rather than the traditional Orr-Sommerfeld linearization. An approximate, order-of-magnitude analysis provides a simple and functionally correct estimate of transition for non-injected acoustic boundary-layers. This technique may prove useful for estimating the stability characteristics of other types of flows.

The computed results for Stokes layers with injection indicate a substantial increase in the acoustic boundary layer thickness for strongly injected laminar or turbulent flows. For injected fully turbulent flows, a pronounced Richardson effect is obtained and is accompanied by very large maximum levels of turbulence ( $> 20\%$ ). Both axial velocity and turbulence profiles exhibit a convected wave train shape. The turbulence development was also found to lag the rectified acoustic velocity by a few degrees at lower frequencies.

Calculated transition results for conventional Stokes layers are in agreement with the approximate analysis and data trends, although at the higher acoustic amplitudes shown by the scaling relation, additional nonlinear effects would be important. The effect of injection is to (nonmonotonically) decrease the critical acoustic Mach number for transition by up to a factor of about three for smooth surfaces. This effect is frequency dependent, but is expressible in terms of the acoustic and injection Reynolds numbers for the problem. The results emphasize the importance of the acoustic and injection Reynolds numbers as the principal similitude parameters for near-surface phenomena.

A further appreciable reduction in critical Mach number (or Reynolds number) is predicted for injection velocities with finite, continuous disturbance levels. This effect is strong enough to indicate that at the minimum critical acoustic Reynolds number, rather modest levels of acoustic pressure ratio ( $\sim 1\%$ ) can induce significant turbulence levels near the surface. It is noted that the theoretical predictions concerning acoustic boundary-layer transition have been recently confirmed by the experiments of Ma, Van Moorhem and Shorthill<sup>28</sup>, although at

relatively low values of injection Reynolds number. Further experiments at values of  $Re_s \geq 1$  are necessary to evaluate theoretical results in regimes characteristic of actual solid rocket combustion.

The potential for turbularization of a near-surface reaction zone in ducted flows such as rocket chambers therefore theoretically exists. However, whether this mechanism can produce instability in such systems depends upon several effects not considered in this investigation. For example, combustion processes and (acoustically) nonlinear behavior such as thermoacoustic streaming could influence the nature of the overall response, while the axial mean flow could bias the transitional characteristics over the acoustic velocity and pressure cycles. Further research on these topics is in progress.

The analysis presented in this work has attempted to identify and quantify some aspects of the role of acoustically induced turbulence in the combustion response of solid propellants. Despite several simplifying assumptions, a complex nonlinear and spatially dependent interaction occurs in the reaction zone which produces a correspondingly complex response function. Some features of the response have long been hypothesized (see, for example, Ref 1.) and are presently analytically confirmed, viz: "full wave" rectification relative to the harmonic acoustic velocity outside the boundary layer, the occurrence of a threshold acoustic amplitude for significant response, and the appearance of a time-mean augmentation ("D-C shift") of the propellant regression rate. Additionally, the magnitude of the response is quite sensitive to propellant "formulation variables"; surface roughness and gas phase heat of reaction (flame-zone thickness) being those assessed in this study.

The results also indicate differences with some prevailing conceptual aspects of velocity coupled response. These include:

- 1) The response to acoustic velocity oscillations can be independent of steady state erosive burning, as demonstrated by the neglect of an appreciable axial mean flow in this analysis. Consequently, contemporary treatments of velocity response functions which simply perturb an erosive burning response would omit an important additional contribution and physical mechanism.

- 2) For nominal combustion parameters, the susceptibility to acoustic transition and propellant response increases with increasing mean pressure.
- 3) The appreciable phase shift of the regression rate response relative to the harmonic external axial velocity can yield a significant "apparent" pressure response, if an attempt was made to analyze this with conventional linear theory.
- 4) The behavior of the velocity response, even at moderate acoustic pressure amplitudes of a few percent, is highly nonlinear and possesses significant harmonic content.

The present results have been obtained utilizing several simplifying assumptions, some of which pose significant research issues in their own right (for example, the potential for direct acoustic-turbulence interaction, or the potential for extreme combustion-turbulence interaction from composite-propellant diffusion flamelets). One of the more intriguing questions posed by the present results is the influence of an axial mean flow interacting with the acoustic boundary-layer and turbulence fields. In this case a substantial biasing of the propellant response over a cycle is anticipated (a necessary condition for instability). Considering the sensitivity and nonlinearity of the acoustic transition process, this area of research could provide special insight into the coupling mechanisms of producing instability in actual devices.

The results presented in this work provide an attempt at evaluating the combined response, due to simultaneous acoustic pressure and (turbulent) velocity oscillations, of the combustion of a solid propellant. An order of magnitude analysis performed on the mean enthalpy equation demonstrated that it and the mean species equation remain similar in the presence of acoustic oscillations in the gas-phase reaction zone. This result should prove useful in future investigations of similar unsteady problems involving premixed combustion, since chemical species transport equations do not have to be solved computationally.

Several of the characteristics of acoustic erosion which have been determined or inferred experimentally using T-burners are presently verified. These include:

- 1) The maximum of acoustic erosion occurs at the velocity antinode (pressure node) and the minimum occurs at the ends of the chamber (pressure antinode). The calculations did not show the negative acoustic erosion (pressure response) near the ends of the chamber as was experimentally reported. The authors believe this discrepancy to be the result of a simplified modeling of the propellant combustion process.
- 2) Under nominal conditions, the threshold velocity of acoustic erosion is less than half the threshold of steady-state erosion.
- 3) Above the threshold value, acoustic erosion is a nearly linear function of the amplitude of the acoustic velocity oscillation.
- 4) The magnitude of the acoustic erosion is a function of the frequency of the acoustic oscillation.

The results have also provided the variation of several characteristics of the combined response as a function of axial location within the chamber. The response of the propellant was found to change from the purely sinusoidal response at the chamber ends to the completely rectified response containing only even harmonics at the center of the chamber. Between these extremes, the frequency content is composed of the fundamental and both even and odd harmonics, which could lead to the excitation of other modes of acoustic oscillation within the chamber of an actual operating system.

## REFERENCES

1. Culick, F. E. C., "A Review of Calculations for Unsteady Burning of a Solid Propellant," *AIAA Journal*, Vol. 6, 1968, pp. 2241-2255.
2. Culick, F. E. C., "Stability of Longitudinal Oscillations with Pressure and Velocity Coupling in a Solid Propellant Rocket", *Comb. Sci. and Technology*, Vol. 2, No. 4, Dec. 1970, pp. 179-201.
3. Lengellé, G., "A Model Describing the Erosive Combustion and Velocity Response of Composite Propellants," *AIAA Journal*, Vol. 13, 1975, pp. 315-322.
4. Brown, R. S., Blackner, A. M., Willoughby, P. G., and Dunlap, R., "Coupling Between Velocity Oscillations and Solid Propellant Combustion," *Journal of Propulsion and Power*, Vol. 2, Sept. 1986, pp. 428-437.
5. Beddini, R. A. "Injection-Induced Flows in Porous Walled Ducts", *AIAA Journal*, Vol. 24, Nov. 1986, pp. 1766-1773.
6. Flandro, G. A., "Non-linear Transient Combustion of a Solid Rocket Propellant," AIAA Paper 83-1269, June 1983.
7. Glick, R. L. and Renie, J. P., "On the Oscillatory Flowfield in Solid Rocket Motors," AIAA Paper 84-1475, AIAA, SAE, and ASME, Joint Propulsion Conference, 20th, Cincinnati, OH, June, 1984..
8. Ben Reuven, M., "The Viscous Wall-Layer Effect in Injected Porous Pipe Flow," *AIAA Journal*, Vol. 24, Feb. 1986, pp. 284-292.
9. Hedge, U. G., Chen, F. L. and Zinn, B. T., "Investigations of Reactive and Non-reactive Acoustic Boundary Layers on Porous Walled Ducts", AIAA Paper No. 85-0235, Jan. 1985.

10. Sankar, S. V., Jagoda, J. I., Daniel, B. R. and Zinn, B. T., "Flame-Acoustic Wave Interaction During Axial Solid Rocket Instabilities," Paper No. 86-0532, AIAA 24th Aerospace Sciences Meeting, January 1986.
11. Baum, J. D. and Levine, J. N. (1986), "Numerical Study of Flow Turning Phenomenon", AIAA Paper 86-0533, Jan. 1986.
12. Merkli, P., and Thomann, H., "Transition to Turbulence in Oscillating Pipe Flow", *Journal of Fluid Mechanics*, Vol. 68, Part 3, April 1975, pp. 567-575.
13. Gostinsev, Yu. A. and Pokhil, P. F., "Relation of Two Combustion Anomalies of Powder Tubes", *Doklady Akademii Nauk SSSR*, (Soviet Physics - Doklady), Vol. 188, No. 1, Sept. 1969, pp. 135-136.
14. Medvedev, Yu. I. and Revyagin, L. N., "Unsteady-State Erosion of a Powder," *Combustion, Explosion, and Shock Waves*, December, 1974, pp. 297-300.
15. Crump, J. E. and Price, E. W., "Effects of Acoustic Environment on the Burning Rate of Solid Propellants," *AIAA Journal*, Vol. 2, 1964, pp. 1274-1278.
16. Corner, J., "The Effects of Turbulence on Heterogeneous Reaction Rates," *Transactions of the Faraday Society*, Vol 43, 1947, pp. 635-642.
17. Crump, J. E. and Price, E. W., "Effect of Acoustic Environment on the Burning Rate of Double-Base Solid Propellants," *ARS Journal*, vol. 31, July 1961, pp. 1026-1029.
18. Beddini, R. A., "A Preliminary Investigation of Fluid Dynamic Aspects of Combustion Instability in Solid Propellant Rocket Motors," U.S. Air Force Rocket Propulsion Lab., Edwards AFB, CA, TM82-01, Dec. 1981.
19. Lin, C. C., "Motion in the Boundary Layer with a Rapidly Oscillating External Flow", *Proceedings of the International Congress on Applied Mechanics*, Vol. 4, University of Brussels, Brussels, Belgium, 1957, pp. 155-167.

20. Lin, C. C., *Theory of Hydrodynamic Stability*, Cambridge Univ. Press, Cambridge, England, 1955, Chap. 3.
21. Keith, H. G., and Purdy, K. R., "Laminar Forced Convection Under the Influence of a Resonant Acoustic Field," *Proceedings of the 1967 Heat Transfer and Fluid Mechanics Institute*, edited by Libby, Olfe, and Van Atta, Stanford Univ. Press, Stanford, CA, 1967, pp. 298-315.
22. Donaldson, C. duP., "Calculations of Turbulent Shear Flows for Atmospheric and Vortex Motions", *AIAA Journal*, Vol. 10, Jan. 1972, pp. 4-12.
23. Varma, A. K., Beddini, R. A., Sullivan, R. D. and Donaldson, C. duP., "Application of an Invariant Second-Order-Closure Model to the Calculation of Compressible Boundary Layers", *AIAA Paper 74-592*, June 1974.
24. Beddini, R. A., "Aerothermochemical Analysis of Erosive Burning in a Laboratory Solid-Rocket Motor," *AIAA Journal*, Vol. 18, No. 11, November 1980, pp. 1346-1353.
25. Schlichting, H., *Boundary Layer Theory*, 6th edition, trans. by J. Kestin, McGraw-Hill, New York, 1968, p. 421.
26. Beddini, R. A., "Analysis of Injection-Induced Flows in Porous-Walled Ducts with Application to the Aerothermochemistry of Solid-Propellant Motors," Ph.D. Thesis, Rutgers, New Brunswick, NJ, October, 1981.
27. T'ien, J. S., "Oscillatory Burning of Solid Propellants including Gas Phase Time Lag," *Combustion Science and Technology*, Vol. 5, 1972, pp. 47-54.
28. Ma, Y., Van Moorhem, W. and Shorthill, R., "An Experimental Investigation of Velocity Coupling in Combustion Instability", *AIAA Paper 90-0038*, 28th Aerospace Sciences Meeting, Reno, NV, Jan., 1990.



## APPENDIX A: TABLE OF ASSUMPTIONS

### Summary of Assumptions Concerning the Gas and Condensed Phases

#### Gas Phase Assumptions

- a) External body forces and the coefficient of bulk viscosity are negligible.
- b) Effects of radiation are negligible.
- c) Species diffusion due to thermal and pressure gradient effects is negligible, and all binary diffusion coefficients are equal.
- d) The Lewis number is unity.
- e) Specific heats of the chemical species are equal and independent of temperature.
- f) The mean flow Mach number,  $\langle M \rangle$ , is negligible.
- g) The acoustic boundary layer thickness,  $\delta_a$ , is much smaller than the duct radius or transverse dimension.
- h) Combustion of a homogeneous reactant mixture proceeds through a single step, irreversible, chemical reaction.
- i) The gas phase species-average molecular weight is equal to the molecular weight of the mixture at equilibrium.
- h) The turbulent enthalpy correlations above the flame zone are negligible.

#### Condensed Phase Assumptions

- a) The condensed phase is homogeneous.
- b) The condensed phase is stationary in the reference coordinate system.
- c) Material properties are constant.
- d) Species diffusion is negligible.
- e) Radiation effects at the interface and in the condensed phase are negligible.
- f) The surface regression rate is small compared to the gas phase injection velocity.
- g) Subsurface reactions are not present.
- h) Surface regression mechanism is governed by the Arrhenius pyrolysis law.

## APPENDIX B: TABLE OF PROPELLANT PARAMETERS

### Propellant Thermochemical Parameters

$$\begin{aligned}T_f &= 2976 \text{ K} \\c_p &= 1.92 \times 10^3 \text{ J/kg-K} \\W_{av} &= 25.8 \text{ kg/kg-mole} \\T_{Ag} &= 2.0 \times 10^4 \text{ K} \\B_g &= 6.5 \times 10^9 \text{ kg}^{1-\Phi} \text{ m}^{\Phi-1} \text{ s}^{-1} \text{ K}^{-\beta_g} \\\Phi &= 1.10 \\\beta_g &= 0 \\\mu &= 4.42 \times 10^{-7} (T)^{0.65} \text{ kg/m/s/K}^{0.65} \\Pr &= 1 \\T_\pi &= 300 \text{ K} \\L_s^o &= -4.184 \times 10^5 \text{ J/kg (-100 cal/gm)} \\\rho_\pi &= 1700 \text{ kg/m}^3 \\c_\pi &= 1.46 \times 10^3 \\A_\pi &= 2.5 \times 10^7 \text{ kg/m}^2\text{-s} \\T_{A\pi} &= 1.0 \times 10^4 \text{ K} \\\dot{r}^* &= 9.2 \times 10^{-3} \text{ m/s} \\T_s^* &= 700 \text{ K} \\p^* &= 68 \text{ atm} \\n &= 0.55\end{aligned}$$

### APPENDIX C: PUBLICATIONS

Roberts, T.A. and Beddini, R.A., *A Comparison of Acoustic and Steady-State Erosive Burning in Solid Rocket Motors*, submitted to the J. Propulsion and Power, December, 1989.

Beddini, R.A. and Roberts, T.A.: *Response of Solid Propellant Combustion to the Presence of a Turbulent Acoustic Boundary Layer*, accepted for publication in the J. Propulsion and Power.

Beddini, R.A. and Roberts, T.A.: *The Premixed Reactive Turbulent Stokes Layer on a Porous Surface*, in Proc. 1986 Fall Meeting, Combustion Institute (Pittsburg), San Juan, Puerto Rico, December 1986, pp. 66-1:66-4.

Beddini, R.A. and Roberts, T.A.; *Turbularization of an Acoustic Boundary-Layer on a Transpiring Surface*, AIAA Journal, Vol. 26, No. 8, August 1988, pp. 917- 923.